IMPROVING PRECISION AND ACCURACY IN COULOMBIC EFFICIENCY MEASUREMENTS OF LITHIUM ION BATTERIES

by

Toby Mishkin Bond

Submitted in partial fulfilment of the requirements
for the degree of Master of Science

at

Dalhousie University
Halifax, Nova Scotia
October 2012

DALHOUSIE UNIVERSITY

DEPARTMENT OF CHEMISTRY

The undersigned hereby certify that they have read and recommend to the Faculty of Graduate Studies for acceptance a thesis entitled "IMPROVING PRECISION AND ACCURACY IN COULOMBIC EFFICIENCY MEASUREMENTS OF LITHIUM ION BATTERIES" by Toby Mishkin Bond in partial fulfilment of the requirements for the degree of Master of Science.

Dated: October 2, 2012

Supervisor: _____

Readers: _____

_____

_____

Departmental Representative: _____

DALHOUSIE UNIVERSITY

DATE: October 2, 2012

AUTHOR: Toby Mishkin Bond

TITLE: IMPROVING PRECISION AND ACCURACY IN COULOMBIC EFFICIENCY MEASUREMENTS OF LITHIUM ION BATTERIES

DEPARTMENT OR SCHOOL: DEPARTMENT OF CHEMISTRY

DEGREE: M. Sc. CONVOCATION: May YEAR: 2013

_____

Signature of Author

To my friends, family, and my partner Laurie

TABLE OF CONTENTS

LIST OF TABLES

LIST OF FIGURES

ABSTRACT

Lithium-ion batteries have been used extensively over the past two decades in the portable consumer electronics industry. More recently, Li-ion batteries have become candidates for much larger-scale applications such as electric vehicles and energy grid storage, which impose much more stringent requirements on batteries, especially in terms of cell lifetime. In order to develop batteries with improved lifetimes, a means of quickly and accurately evaluating battery life is required. The use of coulombic efficiency (CE) is an important tool in this regard, which provides a way to quantify parasitic reactions occurring within the cell. As more stable battery chemistries are developed, the rates of parasitic reactions occurring in the cell become reduced, and differences in CE among cells become increasingly smaller. In order to resolve these differences, charger systems must be developed which can measure CE with increased precision and accuracy.

This thesis investigates various ways to improve the precision and accuracy of CE measurements. Using the high-precision charger (HPC) at Dalhousie University (built in 2009) as a starting point, a new prototype charger was built with several modifications to the design of the existing HPC. The effect of each of these modifications is investigated in detail to provide a blueprint for the development of next-generation charger systems. This prototype charger shows greatly improved precision and accuracy, with CE results that are approximately four times more precise than those of the existing HPC and over an order of magnitude more precise than high-end commercially available charger systems

LIST OF ABBREVIATIONS USED

μ	Chemical potential in joules per atom
CE	Coulombic Efficiency
DEC	Diethyl carbonate
DMM	Digital multimeter
e	Elementary charge 1.602×10^{-19} C
EC	Ethylene carbonate
EMC	Ethyl methyl carbonate
HPC	High-precision charger
I	Current (further described by subscript)
IRC	Irreversible capacity
LCO	Lithium cobalt oxide, $LiCoO_2$
LiBOB	Lithium bis-oxalato borate
LTO	Lithium titanate, $Li_4Ti_5O_{12}$
MCMB	Mesocarbon microbeads
NCA	$LiNi_{0.8}Co_{0.15}Al_{0.05}O_2$
NMC	$LiNi_{1-x-y}Mn_xCo_yO_2$
OCP	Open circuit potential
PC	Propylene carbonate
ppm	Parts per million
Q	Cell capacity (further described by subscript)
RMS(E)	Root mean square (error)

RTD	Resistance temperature device
SEI	Solid-electrolyte interphase
t	Time (further described by subscript)
T	Temperature
TMOBX	Trimethoxyboroxine
UHPC	Ultra high precision charger
VC	Vinylene carbonate

ACKNOWLEDGEMENTS

I would like to thank Jeff Dahn for providing me with the opportunity to participate in a fascinating and important area of research. This project benefited greatly from the assistance of Chris Burns and Aaron Smith, whose expertise and support have been invaluable. I would also like to thank David Stevens, Nupur Sinha, Simon Trussler, and Hannah Dahn who have all helped significantly with this project.

CHAPTER 1 INTRODUCTION

Lithium-ion batteries have become ubiquitous in our everyday lives since the first commercialized cells were developed in the early 1990s. They are the standard battery technology used in the portable consumer electronics industry due to (among other advantages) their superior energy density and cycle life. Recent interest in Li-ion batteries has focused on larger-scale applications such as electric vehicles and grid energy storage. The improvement of existing Li-ion technology to meet the stringent demands made by these applications has become a major global focus of research.

One requirement that is especially important in this context is improved battery life. The lifetime of a typical consumer Li-ion battery is commensurate with the expected useful lifetime of many consumer electronics (on the order of 2-4 years). Replacing the battery (or the whole device) within this timeframe is considered relatively inexpensive. However, in the case of electric vehicles, where the battery is generally the most expensive component, frequent replacements are prohibitively expensive. In order to overcome this problem, new battery materials and components must be developed which yield longer battery lifetimes.

In order to accomplish this, a means of quickly and accurately evaluating the lifetime of new materials is required. Li-ion battery life is limited by internal parasitic reactions between cell components, which result in a gradual loss of capacity as the battery is cycled or stored at elevated temperatures. The parasitic currents resulting from these reactions can be elucidated by various techniques involving high-precision coulometry. However, as increasingly stable (i.e. longer-lasting) materials are developed,

these currents become very small and a greater degree of precision and accuracy is required than is currently available from commercial charger systems. The Dahn lab has recently developed the High Precision Charger (HPC) at Dalhousie University as part of an effort to address these problems. Using the basic design of the HPC as a starting point, the principal goal of this thesis is to improve the precision and accuracy of capacity measurements through hardware and software modifications. In doing so, a better understanding of the factors which contribute to measurement noise and inaccuracy is also obtained.

Chapter 2 provides a general overview of Li-ion batteries. This includes a discussion of basic operating principles, cell components, and common materials used. Physical properties of Li-ion cells, including possible mechanisms of cell degradation and capacity loss, are also discussed.

Chapter 3 introduces the theory and practice of high-precision coulometry and the basic design principles used to build the Dalhousie HPC. This includes a discussion of sources of experimental error and the state of the art at the beginning of this project.

Chapter 4 describes the design and construction of the new prototype charger system known as the ultra high-precision charger (UHPC). This includes a detailed discussion of the modifications made to the original HPC design. Initial results obtained using the UHPC are also presented.

Chapter 5 provides a detailed evaluation of the UHPC, including a quantitative analysis of the contribution made by each modification to the observed improvements in precision and accuracy. The performance of the UHPC is also compared to that of other charger systems.

Chapter 6 summarizes the general conclusions of this thesis. This includes a discussion of possible future work that would further the research presented here.

CHAPTER 2 LITHIUM-ION BATTERIES

A Li-ion battery is generally composed of multiple cells which are linked together in series and/or in parallel. The basic operating principle of a Li-ion cell is the transport of Li^+ ions between two electrodes which are capable of Li storage.

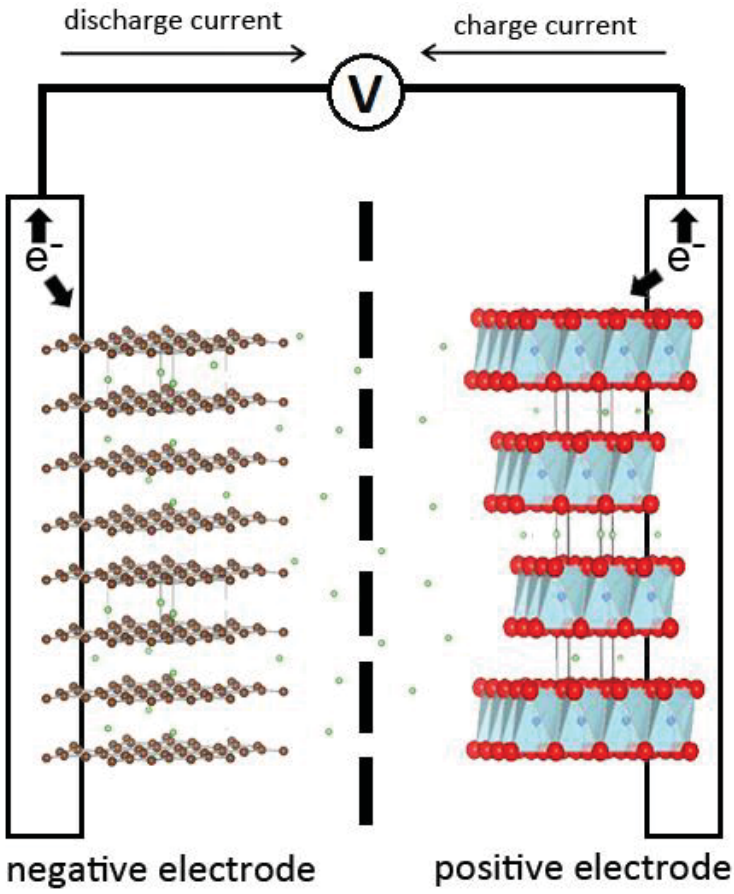

Figure 2.1 A schematic diagram showing the generalized operation of a Li-ion cell. Li^+ ions are indicated by green spheres.

Figure 2.1 shows a diagrammatic representation of a Li-ion cell. Li^+ is transported through an electrolyte solution which is composed of a Li-containing salt dissolved in an organic solvent or conductive polymer. The electrodes are separated by a

electronically insulating polymeric membrane which is ionically conductive (Li^+ permeable) when wetted with electrolyte. The electrodes are composed of materials in which Li is stored at different chemical potentials. The positive electrode stores Li at a lower chemical potential than the negative electrode, giving rise to an overall cell voltage. This voltage is defined as the difference in chemical potential of Li in each respective host material (in joules per Li atom) divided by the elementary charge.

$$V_{cell} = \frac{\mu_{negative} - \mu_{positive}}{e} \tag{2.1}$$

Operating cell voltages are typically in the range of 3.0 V to 4.2 V [1].

When the cell is discharged, Li^+ ions spontaneously move from the negative electrode to the positive electrode. To maintain charge balance, the associated electrons move from the negative electrode to a metal (usually copper) current collector, where current flows through an external circuit into the positive electrode via another current collector (usually aluminum). When the cell is charged, an external power source drives current in the opposite direction, resulting in a potential gradient that causes Li^+ ions to migrate through solution from the positive electrode back to the negative electrode.

The most common mechanism for Li storage is the intercalation of Li^+ ions into the structure of the active material, where ions are reversibly inserted into vacant sites with minimal change in the material's overall structure. As a result, operation of the cell is highly reversible, with little expansion and contraction of the electrode. Most intercalation compounds are layered structures where Li is intercalated between layers of the electrode material [1].

The capacity of a cell refers to the amount of charge that can be stored, and is generally expressed in milliamp hours (mAh) in battery literature. The theoretical capacity of an electrode material is usually denoted by its specific capacity, which is typically expressed in milliamp hours per gram of active material (mAh/g). The total energy of a cell is the product of the cell's voltage and capacity.

Instead of denoting current as an absolute quantity in amperes, it is more common in battery literature to express current as a fraction of cell capacity. In this notation, a fraction of capacity (denoted by *C*/*X*) is used to denote the amount of charge transferred over one hour. For example, a cell being charged at a rate of C/20 would take 20 hours for a complete charge or discharge to take place. Commercial cells are often developed as either "energy cells" (high voltage and high capacity) or "power cells" (high voltage and good rate capability) [1].

2.1 Electrode Materials

A wide variety of positive and negative electrode materials are commonly used in Li-ion batteries. Instead of using the chemical potential to indicate the energy state of Li in a given host material, it is more common to use the electrochemical potential with Li/Li^+ as a reference. Negative electrodes will undergo Li intercalation at low potentials vs. Li/Li^+ (high chemical potential) compared to positive electrodes, in which intercalation occurs at high potentials vs. Li/Li^+ (low chemical potential). An electrode material cannot operate at a potential more negative than Li/Li^+, as ions would simply be reduced to Li metal. To achieve greater cell voltage, it is thus generally desirable for

negative electrode materials to intercalate Li at potentials which are as low as possible. Likewise, it is desirable for positive electrode materials to intercalate Li at potentials that are as high as possible.

In addition to having desirable voltage and capacity, there are several other important properties of a good electrode material. The material must be able to intercalate Li^+ reversibly without significant structural changes that can cause physical damage to the electrode with repeated cycling. Electrodes must also be insoluble in the electrolyte with which they are to be used, and must be stable enough in the cell environment so as not to pose a safety risk. The electrode should also be electrically conductive, as well as have good Li^+ diffusivity [1]. All of this must be achieved at a cost that is acceptably low.

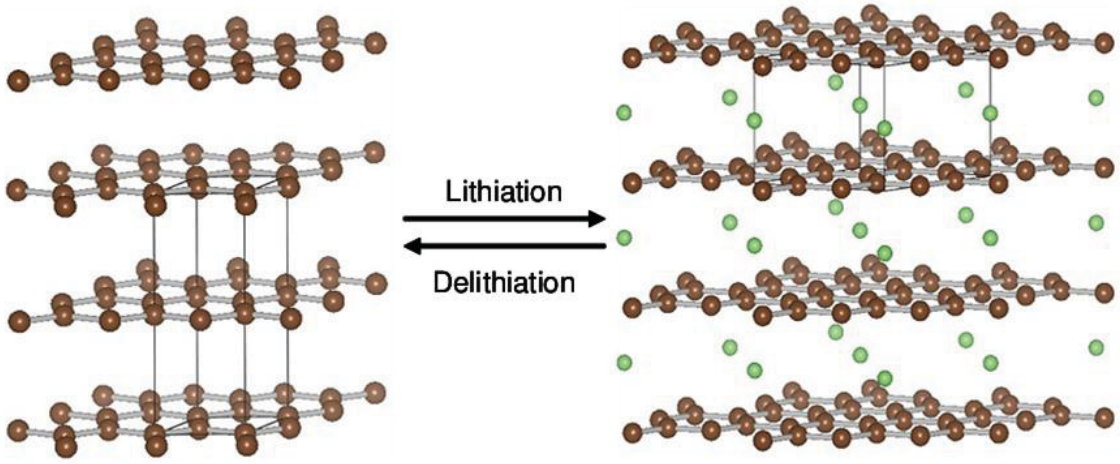

Figure 2.2 The structure of graphite shown in its fully lithiated and fully delithiated state. Carbon atoms are brown and lithium atoms are green.

The most common negative electrode found commercially is graphite, as it is a well understood, cheap, and stable material with a low potential (0.1-0.3 V vs. Li/Li^+) and large specific capacity (up to 372 mAh/g) [2]. Figure 2.2 shows the structure of

graphite, which consists of layered sheets of graphene that are usually arranged in an ABAB stacking pattern. When fully lithiated, the resulting composition is LiC_6. Synthetic graphite generally offers better performance than naturally occurring graphite, but its behavior and properties depend significantly on the method of preparation [1]. Some Li-ion batteries (including the graphite-containing cells used in this thesis) use graphite in the form of Mesocarbon Microbeads, (MCMB) which are uniform graphitic particles, offering high specific capacity and relatively low surface area (improving stability and safety properties).

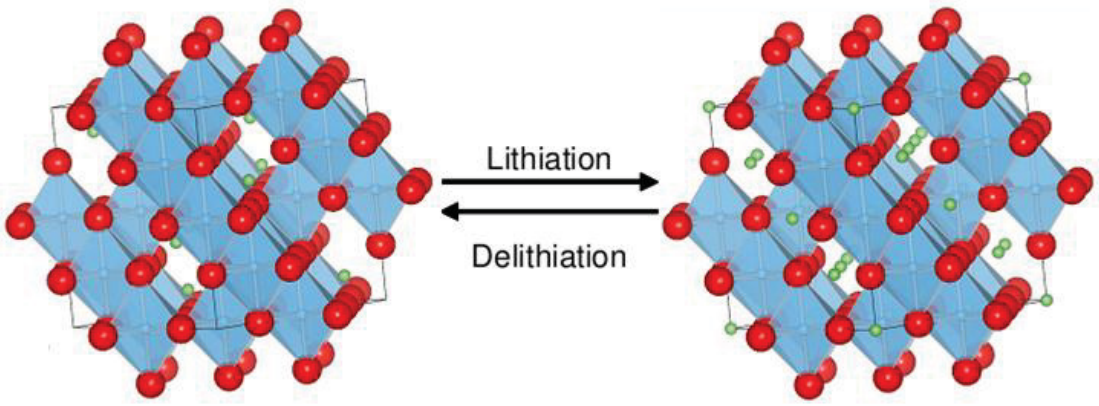

Figure 2.3 The spinel structure of lithium titanate in its fully lithiated and partially delithiated state. Oxygen atoms are red, titanium atoms are blue, and lithium atoms are green. $1/6^{th}$ of the sites shown to be completely occupied by titanium atoms are in fact randomly occupied by Li.

Another common negative electrode material is lithium titanate, $Li_4Ti_5O_{12}$ (LTO). Figure 2.3 shows the spinel structure of LTO, where Li^+ is intercalated into a network of tunnels. LTO has a much lower specific capacity than graphite (175 mAh/g) and operates at an average potential that is 1.4 V higher, resulting in full cells with

diminished voltage [3, 4]. It also costs significantly more to produce than graphite, and is consequently not nearly as common in commercial cells. However, LTO is very stable and exhibits excellent cycle life, making it ideal for applications where longevity is the principal consideration. Most of the batteries used in this thesis were LTO-based cells provided by Medtronic Inc., a company that designs and manufactures medical implants (an application in which battery life is certainly of great importance).

Graphite and LTO were the only negative electrode materials used in this thesis, but others are also available. Li metal can itself be used as a negative electrode, however its morphology changes as the cell is cycled, leading to the formation of dendrites [1]. This limits cycle life and constitutes a major safety concern, so rechargeable batteries based on Li metal are not commercially available. However, Li-metal-based cells are commonly used in research, where Li metal is paired with another electrode material so as to isolate and study the materials behavior (this is known as a "half cell"). Other negative electrode materials based on Si and Sn are also the focus of world-wide research, but are not discussed here.

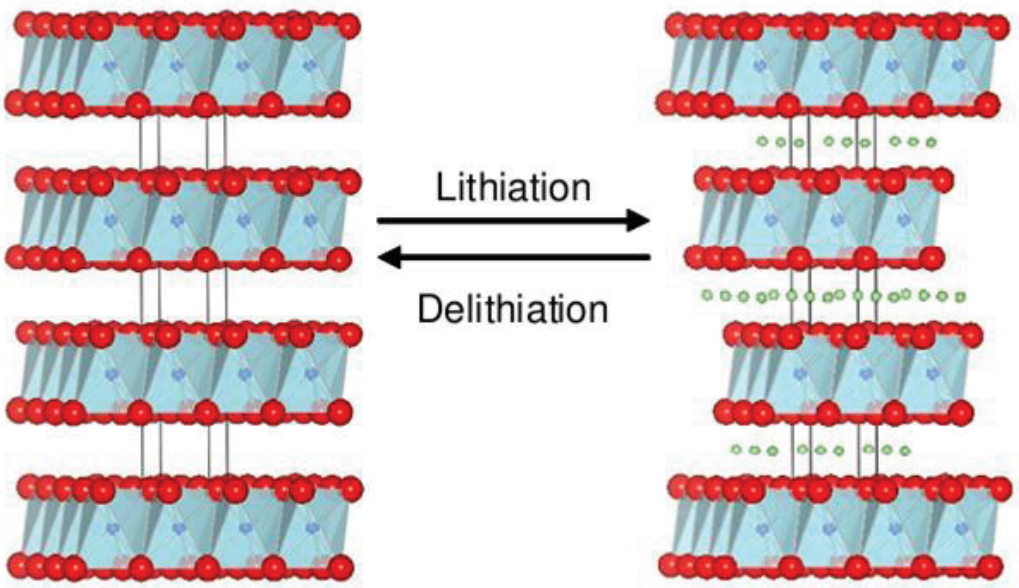

Figure 2.4 The structure of $LiCoO_2$ in fully lithiated and delithiated state. Oxygen atoms are red, cobalt atoms are blue, and lithium atoms are green.

Numerous positive electrode materials are commonly used, most of which are lithium metal oxides that are also composed of layered or spinel-type structures. Layered and spinel positive electrode structures are generally described by the formulas, $LiMO_2$ and LiM_2O_4, respectively (where M is one or more transition metals, typically Co, Mn, Ni, etc.). The first commercial Li-ion cells developed by Sony used $LiCoO_2$, (LCO) which is still the most common positive electrode material currently used in commercial batteries [1]. The layered structure of $LiCoO_2$ is shown in Figure 2.4. Since Co is fairly expensive, materials composed partially or fully of other metals are often used to reduce cost, such as $LiNi_{1-x-y}Mn_xCo_yO_2$ (NMC) or $LiMn_2O_4$ (a spinel material). Other compositions can yield improvements in specific capacity, such as $LiNi_{0.8}Co_{0.15}Al_{0.05}O_2$ (NCA). There are several other positive electrode materials used which yield different advantages for specific applications, but in the interest of simplicity, $LiCoO_2$ is the only positive electrode material used in this thesis.

2.2 ELECTROLYTES

The most common type of electrolyte system in Li-ion batteries consists of a Li-containing salt dissolved in one or more organic solvents. Polymer-based electrolytes can also be used [1]. The most common type of salt used is $LiPF_6$, as $LiPF_6$ solutions display high ionic conductivity on the order of 10^{-2} S/cm as well as a high lithium ion transference number (the fraction of current that is carried by Li^+) of 0.35 [1]. Other salts used include $LiBF_4$, $LiN(CF_3SO_2)_2$, and lithium bis-oxalato borate (LiBOB). Li salt concentration is typically close to 1.0 M, as this provides optimal ionic conductivity (as viscosity becomes a limiting factor at higher concentrations).

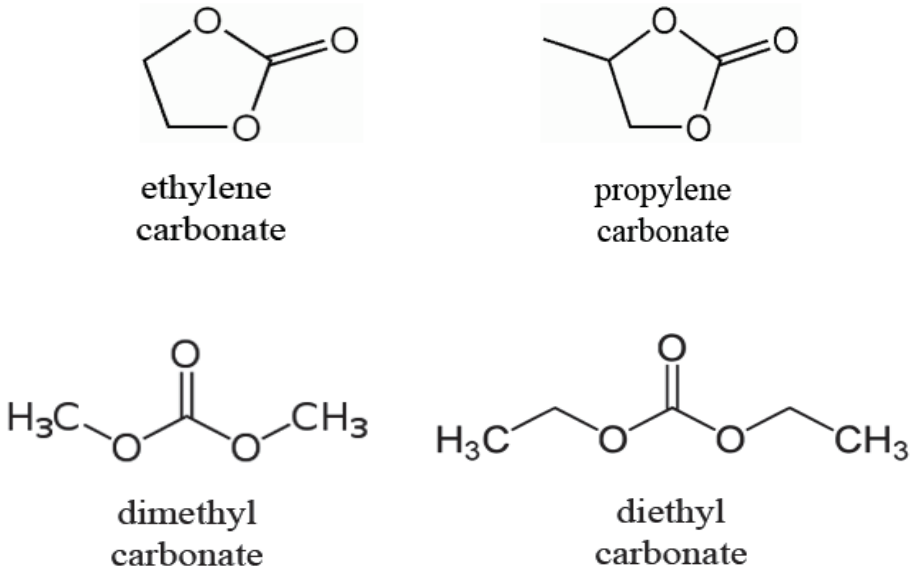

Table 2.1 Structures of some common carbonate-based solvents used in Li-ion battery electrolyte solutions.

Solvents used in Li-ion batteries cannot be aqueous, as water is not electrochemically stable at the potentials present in most Li-ion cells. Instead, organic

solvents are used which are chemically and electrochemically stable under cell conditions. Solvents used in Li-ion cells are almost exclusively carbonate-based, as they possess a high dielectric constant while being able to effectively solvate Li^+ (due to their polar, aprotic structure). Different solvents or mixtures of solvents can be chosen depending on their chemical behavior with respect to different electrode materials. For example, propylene carbonate (PC) can degrade graphite electrodes when used alone, but is stable when combined with ethylene carbonate (EC) or diethyl carbonate (DEC) [1]. Table 2.1 lists some of the most common solvents used. Interactions between electrode materials and the electrolyte can be complex, and are discussed in the next section.

2.3 Potential Mechanisms of Capacity Loss

Capacity loss in Li-ion batteries is the result of parasitic reactions which consume active components of the cell. A detailed understanding of these reactions is necessary for researchers who are developing materials and additives which are designed to improve cell life. A brief overview of these reactions is presented here in the interest of providing a physical context for the discussion of cell decay.

2.3.1 The Solid-Electrolyte Interphase

In Section 2.2, it was mentioned that carbonate-based solvents are commonly used because they tend to be stable with respect to most electrode materials. In actuality, this stability is the result of a passivation effect, whereby electrolyte reacts at the

electrode surface to form a layer known as the solid-electrolyte interphase (SEI). Capacity loss results from the formation of the SEI because both solvent and Li^+ (which are in finite supply in the cell) are incorporated into its structure, rendering them electrochemically inactive [5].

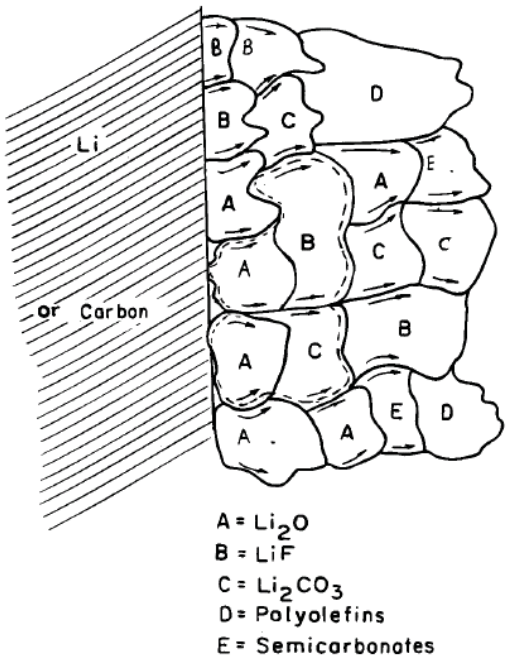

Figure 2.5 A diagram representing the heterogeneous structure of the SEI [5].

The structure of the SEI is amorphous and heterogeneous, with its actual composition being dependent on the specific electrode material and electrolyte formulation being used [6]. The example shown in Figure 2.5 consists of common SEI products which result from the reaction of $LiPF_6$ and carbonate-based solvents with a negative electrode.

When a newly constructed cell is first cycled, there is a sharp drop in capacity (known as the irreversible capacity, or IRC) as the initial SEI is formed, consuming a significant amount of electrolyte. Subsequent growth and repair of the SEI continues to a

lesser degree as the cell is cycled [5]. In a closed cell with a finite supply of electrolyte, this will eventually lead to electrolyte depletion and battery will cease to function. Battery manufacturers generally perform an initial cycling regime to form the SEI of new cells under controlled conditions before they are shipped to market. The stability of electrolytes and additives with respect to a given electrode material is the result of a uniform, stable SEI with controlled growth after the IRC.

2.3.2 Electrolyte Oxidation and Electrode Damage

Another way in which electrolyte can be depleted is by oxidation at the positive electrode [7]. As discussed earlier, positive electrodes with high potentials are desirable as they maximize the cell voltage (increasing energy and power). However, using materials even as positive as $LiCoO_2$ (which operates at a nominal potential of 4.0 V vs. Li/Li^+) can lead to oxidation of carbonate species used in common electrolytes [8]. As with the SEI, the products of these reactions are complex and dependent on the materials and electrolytes being used. There are several different mechanisms by which electrolyte oxidation can proceed, with varying effects on cell capacity. Since electrolyte oxidation occurs only at the positive electrode, it can proceed under open-circuit conditions, resulting in a drop in the open-circuit potential (OCP) of the cell (commonly referred to as self-discharge).

Apart from the consumption of active electrolyte, electrode materials can themselves be damaged during cell operation. Some electrode materials which are more prone to volume expansion during intercalation can be mechanically damaged (through

cracking, etc.) such that parts of the electrode may lose electrical contact with the rest of the cell [9]. Another way that electrode damage can occur is the dissolution of transition metals from positive electrode materials. When a positive electrode is delithiated, the oxidation state of the transition metals in the structure must become more positive in order to maintain charge neutrality. This can result in the oxidized transition metal ions being dissolved in the electrolyte and deposited on the negative electrode surface.

2.4 Measuring Capacity and Coulombic Efficiency

When a Li-ion cell is cycled using a charger, it is normally charged and discharged at a constant current between two fixed voltage limits (at which the polarity of the current is switched). The exact shape of these voltage curves is dictated by the underlying intercalation behavior of Li^+ in the specific electrode materials being used. In general, the cell voltage increases as more Li^+ ions move from the positive electrode to the lower-potential negative electrode (charge) and decreases as ion move from the negative electrode back to the positive electrode (discharge).

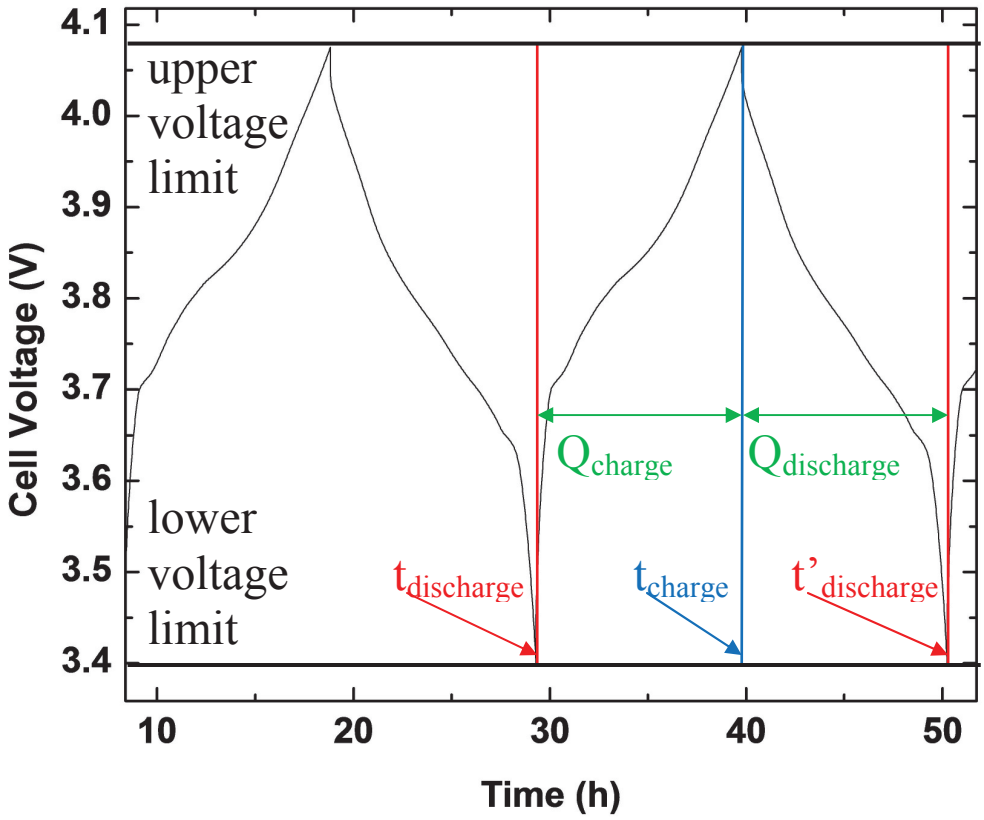

Figure 2.6 Cell voltage of a graphite/LCO cell over time as the cell is cycled between fixed voltage limits of 3.4 V and 4.075 V at a constant rate of C/20. Integration limits for calculating charge and discharge capacity (Q_{charge} and $Q_{discharge}$) are shown.

Figure 2.6 shows an example of a voltage vs. time curve for a graphite/LCO cell. The capacity of the cell is calculated by integrating current over time, using the voltage endpoints to determine the limits of integration. Capacity is calculated separately during charge and discharge. Using the notation shown in Figure 2.6, the charge and discharge capacities are defined as follows:

$$Q_{\text{charge}} = \int_{t_{\text{discharge}}}^{t_{\text{charge}}} I(t)dt \qquad Q_{\text{discharge}} = \int_{t_{\text{charge}}}^{t'_{\text{discharge}}} I(t)dt \tag{2.2}$$

Successive cycles would be calculated accordingly. The precise, experimental determination of these integration limits is non-trivial and is discussed in detail throughout subsequent chapters. The term "capacity fade" is often used to describe how the discharge capacity changes from one cycle to the next,

$$\text{capacity fade} = Q_n - Q_{n-1} \tag{2.3}$$

Where "*n*" refers to cycle number, "Q_n" refers to the discharge capacity measured for cycle "n", and "Q_{n-1}" refers to the discharge capacity for the directly preceding discharge.

Due to the presence of previously discussed parasitic reactions, any given pair of charge and discharge capacities will not be equal. This asymmetry is quantified by a cell's coulombic efficiency, (CE) which is defined for a full cell as the ratio of a given discharge capacity to its immediately preceding charge capacity:

$$CE = \frac{Q_{\text{discharge}}}{Q_{\text{charge}}} \tag{2.4}$$

CE values that are closer to unity (1.00000…) indicate a lower degree of parasitic reactions [8]. A CE that is exactly equal to unity would imply that there are no parasitic reactions occurring in a cell and that it will cycle indefinitely. The importance of measuring CE has also been recognized in past battery literature, a notable example being a 1995 paper by Ohzuku *et al.* [10] which stated that negative and positive electrodes with matched CE could yield excellent cycle life, even if CE was less than unity (though the cells in this experiment contained a large excess of electrolyte, which would not show the capacity fade due to electrolyte depletion seen in commercial cells).

The alternative to using a predictive method like this would be to test cells by cycling them until they "die," which would require unacceptably large amounts of time. However, as cells are developed that are more stable with lower rates of parasitic reactions, CE values will move closer and closer to unity and differences between cells will also become continually smaller. Such differences will be increasingly difficult to resolve with existing instrumentation. The development of a charger system that can measure CE with the highest possible precision and accuracy is the main thrust of this thesis.

2.5 Summary

This chapter is meant to give a broad introduction to the field of Li-ion battery science and to provide a chemical and physical context for the discussion of high-precision coulometry and the data that is presented in this thesis. A more quantitative and

detailed discussion of high-precision coulometry, including a description of the current state of the art, is presented in the following chapter.

CHAPTER 3 HIGH-PRECISION CE MEASUREMENTS

The components required to construct a charger system are (at a minimum) a current source, a voltmeter, and a computer or other processing device to control the system. A computer monitors cell voltage, measures time, and controls the output of the current source. Many large-scale commercial charger systems are available on the market, and are commonly used in industry for research and quality assurance. However, these commercial systems are generally incapable of measuring CE with enough precision to study cells with very good stability. This is reflected in the high level of scatter found in CE data that is reported in the literature. A paper by Li *et al.*, [11] which investigated the CE of silicon/graphite/carbon composite electrodes in different electrolytes, and a paper by Yi *et al.*, [12] which investigate the CE of various positive electrode materials in half cells give examples of this. Both of these papers show CE data with scatter of more than ±0.5%. This level of precision is insufficient for the investigation of highly stable Li-ion batteries, many of which yield CE data that is well above 99.95%. Examples of such cells are shown in subsequent chapters. This chapter will discuss the experimental factors which contribute to error in capacity/CE measurement, as well as describe the design and construction of a high precision charger (HPC) system that was developed in the Dahn lab in 2009. An understanding of this system is important, as the HPC represents the starting point for the work presented in this thesis.

3.1 Factors Affecting Error in CE Measurement

There are 4 main experimental factors which contribute directly to the error associated with measuring capacity and CE. These are summarized in Table 3.1.

Parameter	Associated Error	Desired Error in Q	For C/10 rate measurements	For C-rate measurements
ΔI	$\Delta Q = \Delta I\ t$	< 0.01%	ΔI < 0.01%	ΔI < 0.01%
ΔV	$\Delta Q = (dQ/dV)\ \Delta V$	< 0.01%	ΔV < 0.0001 V	ΔV < 0.0001 V
Δt	$\Delta Q = I\ \Delta t$	< 0.01%	Δt < 3.6 s	Δt < 0.36 s
ΔT	$\Delta Q = (dV/dT)(dQ/dV)\ \Delta T$	< 0.01%	ΔT < 1°C	ΔT < 1°C

Table 3.1 List of factors which contribute to measurement error of capacity and CE, where Q is cell capacity, I is the charge/discharge current, V is cell voltage, Δt is the time interval between voltage measurements, and T is the temperature of the cell [14].

In Table 3.1, ΔI refers to error associated with the output of current sources; ΔV denotes the error associated with measuring cell voltage; Δt is the time interval between cell voltage measurements; ΔT is the variation in temperature of the cell. In order to achieve an error in capacity measurement that is less than 0.01%, each of these values must be within the limits indicated in Table 3.1. In order to calculate these maximum error values, assumptions are made with regards to dQ/dV (the amount of charge transferred over a given change in cell voltage) and dV/dT (the change in cell voltage as a result of a change in cell temperature). For the calculated values shown, dQ/dV is assumed to be the entire cell capacity over 1 V (Q/1) and dV/dT is assumed to be 100 μV/°K [14]. Figure 4.1 shows a graphical representation of these error values and illustrates how each of them must be minimized in order to precisely and accurately determining endpoints to calculate capacity.

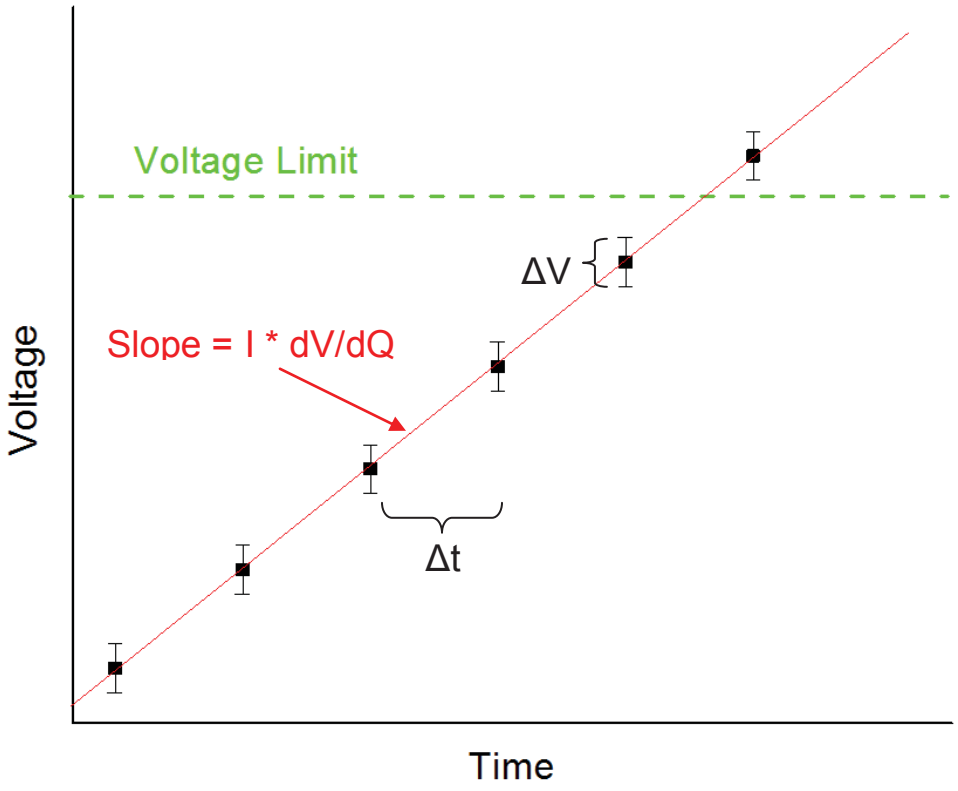

Figure 3.1 A graphical representation of some of the error values defined in Table 3.1.

In order to optimize performance according to these criteria, a charger should be built using accurate current sources with low-noise output and voltmeters that can measure cell voltage accurately and precisely at a high sample rate. A high-precision charger must also provide some means of minimizing temperature variation of cells as they are being cycled. These are the basic design principles that were used by the Dahn lab to build the high precision charger (HPC) at Dalhousie University in 2009-2010 [13].

3.2 Design and Construction of the Dalhousie HPC

The HPC is a 60-channel charger system that is made up of commercially manufactured current sources and digital multimeters (DMMs). The HPC was constructed in the Dahn lab by graduate students, Aaron Smith and Chris Burns (along with a number of co-op students). After reviewing potential current sources and DMMs according to the criteria listed in Table 3.1, the decision was made to use Keithley 220 current sources and Keithley 2000 Scanning DMMs, due to their excellent precision and accuracy specifications (see Table 3.2). Newer-model Keithley 6220 current sources were also used, but the 220s were preferred as they could be purchased used for a fraction of the price. Figure 3.2 shows the entire HPC as completed in 2010.

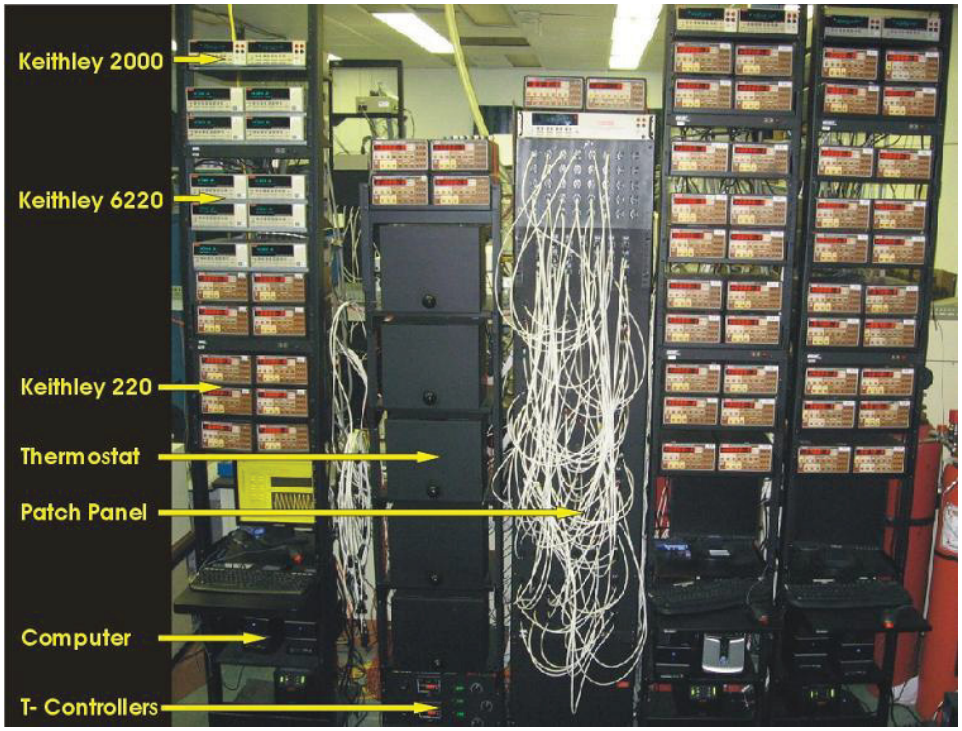

Figure 3.2 The Dalhousie HPC as constructed in 2010, with instruments and components as indicated.

The instruments of the HPC were connected to computers using the GPIB IEEE interface, with data acquisition and instrument control being performed by software (written by Aaron Smith). The HPC is divided into 6 separate 10-channel systems, each with 10 dedicated current sources, a computer, and 1 DMM which scans the cell voltage of all 10 channels in sequence. Batteries were housed in temperature-controlled boxes which could each be set to different temperatures. A patch panel allowed any given channel to be connected to any given slot in a temperature-controlled box.

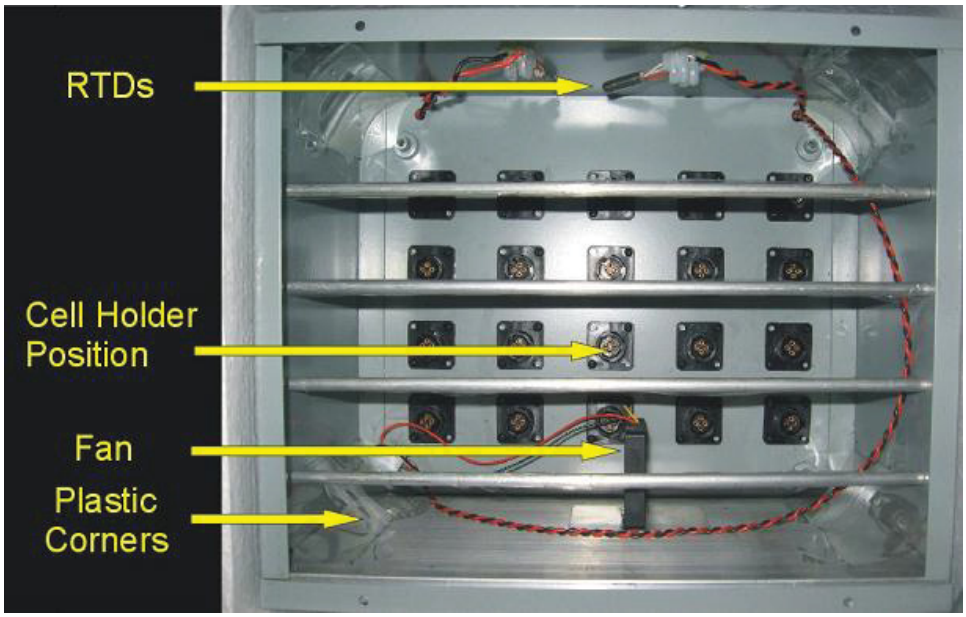

Figure 3.3 The inside of a box used to house cells during cycling. Resistance-temperature devices (RTDs) are used to measure temperature and control heating elements in the box. Cells are placed in modular units which are connected to sockets mounted on the back wall of the box.

The inside of one of these temperature-controlled boxes is shown in Figure 3.3. The box consisted of a steel enclosure that was fixed inside another larger steel enclosure, with polyurethane insulation filling the space between them. The inner enclosure was also wrapped in heating tape, which was controlled by a resistance-temperature device (RTD)

placed on the top wall inside the box. A small 60 mm computer fan was used to circulate air in the box to avoid the formation of temperature gradients. The resulting temperature variation inside the box was kept to within 0.1°C [13].

Table 3.2 shows the resulting specifications of the HPC as described in comparison to the specifications of other commercially available charger systems.

Manufacturer	Current Resolution	Voltage Resolution	Current Accuracy	Voltage Accuracy	Time Between Measurements (seconds)
Maccor 4000 Series	16 bit	16 bit	0.02-0.05% of full scale	0.02-0.05% of full scale	0.01
Arbin BT2000	16 bit	16 bit	0.02-0.05% of full scale	0.02-0.05% of full scale	0.1
Bitrode MCV	100 nA	100 μV	0.1% of full scale	0.1% of full scale	0.1
Neware BTS-5V1mA	16 bit	16 bit	0.05% of full scale	0.05% of full scale	5
Lisun PCBT-100-32D	0.1%	0.1%	<0.5%	<0.1%	1
Land CT2001	0.1%	0.1%	N/A	N/A	N/A
Xeno WBCS 5000	16 bit	16 bit	N/A	N/A	0.05
Biologic VMP	0.0003%	16 bit	0.05%	0.1%	0.02
Dalhousie HPC	0.005%	10 μV	0.05%	0.0025% of range	5

Table 3.2 Specifications of various commercially available charger systems, including the Dalhousie HPC [13].

In Table 3.2, many of the specified errors are given as percentages of full scale. For example, the Maccor Series 4000 charger has a full-scale voltage range of 5 V, yielding a

voltage resolution of (at best) 1 mV. The term "16 bit" corresponds to 1 part in 2^{16} (1 part in 65536 or 0.0015%) of full-scale. For example, the voltage resolution of the Maccor Series 4000 is 75 μV (0.0015% of 5 V). One of the important current source specifications that this table does not capture is the relative accuracy of charge and discharge current outputs. Since CE is defined as the ratio of discharge and charge capacities, the absolute accuracy of current source output is not particularly important as long as the charge and discharge currents are sufficiently matched. If there is a discrepancy between the magnitude of charge and discharge currents, this will lead to a shift in CE data and a loss of accuracy. One of the advantages of the Keithley 220 current sources is that this charge/discharge balance can be directly calibrated so that the difference between charge and discharge current output is well within 0.01%.

All of the specifications for the Dalhousie HPC exceed the requirements listed in Table 3.1 with the exception of the 5-second time interval between voltage measurements. The Keithley 2000 DMM was set to wait for an interval of 500 ms for each channel so as to ensure that the voltage reading had stabilized. Since each DMM must scan sequentially through 10 channels and wait 500 ms at each channel, a time interval of at least 5 seconds elapses before the DMM scans a given channel again. This time interval was greater than the 3.6 seconds indicated in Table 3.1, but this limitation is overcome using a software interpolation procedure to determine charge and discharge endpoints. This is discussed in detail in section 3.4.

3.3 Quantifying Precision and Accuracy of CE Data

In order to quantitatively assess the performance of a charger system, CE data was fit via least squares regression. All fitted CE data in this thesis used a 2nd-order polynomial (parabolic) fitting function. This was done to account for long-term curvature that is commonly seen in CE data, which is the result of changes in the rates of parasitic reactions (such as the decreasing rate of SEI thickness growth). The use of a quadratic fitting function is not intended to provide a predictive model of CE behavior, but simply to account for this natural curvature using a function with the fewest possible fitting parameters. The first few data points from new cells were often excluded from the regression, as they did not generally fit well to a parabolic curve. Figure 3.4 shows an example of CE data that has been fit.

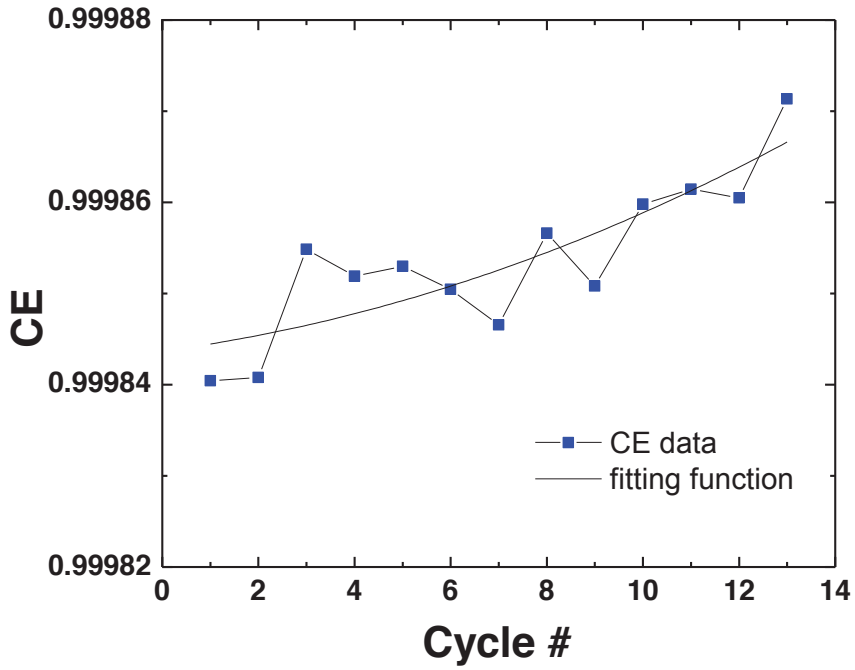

Figure 3.4 An example a 2nd-order polynomial fitting function that has been produced using least-squares regression from the CE data shown.

Random oscillations above and below the fitting function are considered to be random noise due to measurement error, referred to in this thesis as "scatter."

From these polynomial regressions, various statistical parameters could be determined. The parameter used to quantify CE scatter is the root mean square error (RMSE or RMS error) which is defined here as follows:

$$RMSE = \sqrt{\frac{\sum (x_i - x_f)^2}{n}} \qquad 3.1$$

where x_i refers to a value from the data set used for the regression, (which, in this case, would be the CE data) x_f is the value given by the fitting function at the same cycle number as x_i, and n is the number of data points used in the regression. RMSE represents the magnitude of the average difference between the data set and the fitting function, and can be regarded as the standard deviation of the data (using a function as the average value instead of a constant). Thus, a smaller RMSE value indicates better precision in CE data.

The determination of accuracy is often a relatively simple matter for many analytical instruments. Generally, some sort of analytical standard is available that displays well-established, measurable properties. Unfortunately, there is no such convenient standard available that displays a well established, constant CE. This makes the determination of the accuracy of a charger system non-trivial. The accuracy of the various components can be optimized through proper calibration, (using a voltage

standard to calibrate DMMs, for example) but assessing the accuracy of the charger system as a whole is more involved.

Although there is no single analytical standard for CE as such, the accuracy of a charger system can still be quantified by examining the variation between datasets taken from different channels. Ideally, if a set of perfectly identical cells were run under identical conditions on different channels of a charger, then relative shifts between these datasets could be attributed to differences in the behavior of each channel (such as discrepancies in current source output). In reality, no set of cells will be exactly identical, and observed shifts between CE data are the result of both channel-to-channel and cell-to-cell variation. The deconvolution of these two factors is, at best, exceedingly difficult. Although no set of cells can in practice be perfectly identical, commercially made cells can be used which are the product of a mechanized, reproducible, quality-controlled manufacturing process. This minimizes the contribution of cell-to-cell variation, allowing for the assumption that discrepancies between data from different channels can mostly be attributed to measurement error. In the remainder of this thesis, the term "channel-to-channel variation" is used to denote what is in fact the sum of both channel-to-channel and cell-to-cell variation.

The performance of the HPC was characterized using 10 pairs of wound prismatic cells with various additives. This experiment was performed before the beginning of this thesis. The results of this data are shown in Figure 3.5.

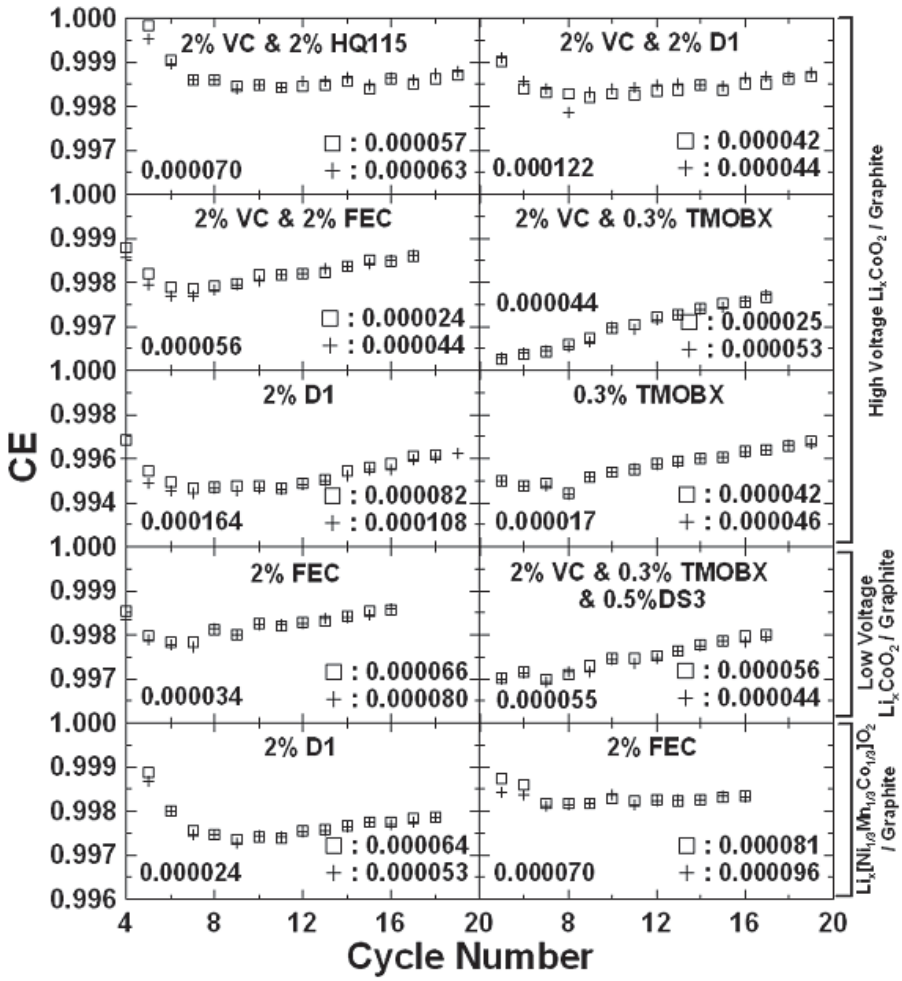

Figure 3.5 CE data from 10 pairs of commercially manufactured wound prismatic cells that were tested on the HPC in 2011. Electrode materials are indicated to the right and additives used in each pair are indicated on the appropriate panel. RMS error values for each pair are indicated on the bottom-right corner of each panel and channel-to-channel variation is indicated on the bottom left.

RMS error values from this experiment were as low as 24 ppm (0.000044 or 0.0044%) and as high as 108 ppm. The average RMS error of all the cells combined is 59 ppm. Channel-to-channel variation is calculated by producing polynomial fitting curves for data sets collected from separate channels running the same type of cell. The RMS error between these fitting functions was then calculated (i.e. the root mean square difference between each corresponding point of the 2 functions). The results of this

calculation varied from 24 ppm to as high as 164 ppm, with an average of 65 ppm for all the data shown. In this thesis, when channel-to-channel variation is calculated for more than two channels, the fitting functions of the outermost two datasets of a group (highest and lowest average CE) are used to perform the procedure described above.

3.4 Endpoint Determination and Correction

Since any charger system must collect voltage data at a finite sample rate, cells will always be charged to a voltage that slightly exceeds the predetermined limit. In the case of the HPC, voltage data was collected every 5 seconds, resulting in charging or discharging past the voltage limit for a duration between zero and 5 seconds. However, this limitation can be overcome by correcting for the resulting voltage limit overshoot in data post processing.

After raw data is collected from the charger, capacity and CE values are calculated for each cycle using in-house software written for this purpose. In order to determine the exact time at which the cell voltage crosses the voltage limit, the last data point of the cycle (which exceeds the voltage limit) and the data point directly preceding it (which is within the voltage limit) are used to define a linear function, which can be used to interpolate where the voltage limit was crossed.

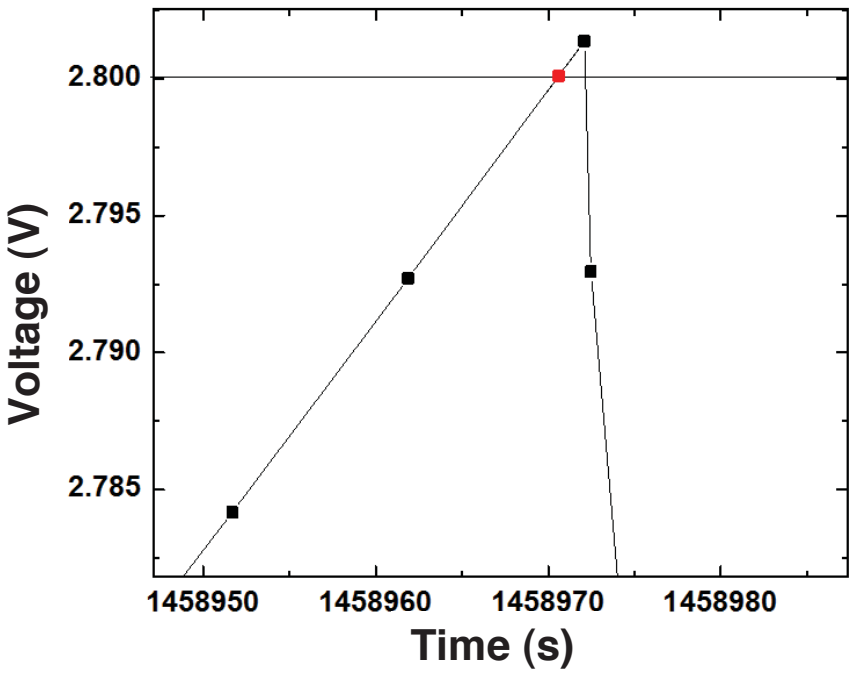

Figure 3.6 A graph illustrating the charge endpoint determination for a LTO/LCO cell running on the HPC. The data in black represents the measured data collected from the HPC, while the red data point indicates the point at which the voltage limit is crossed (determined by linear interpolation).

Figure 3.6 shows an example of this linear interpolation using real data collected on the HPC. The point at which the voltage limit is crossed is calculated by finding the intersect between the interpolated linear function and the voltage limit. The time at which this occurs is then used when calculating capacity.

Although this interpolation procedure allows for more accurate determination of endpoints, the overshoot of voltage limits also results in extra charge that is transferred after the voltage limit has been crossed. This excess charge must be corrected for in order to accurately calculate capacity. Figure 3.7 illustrates how this correction is carried out.

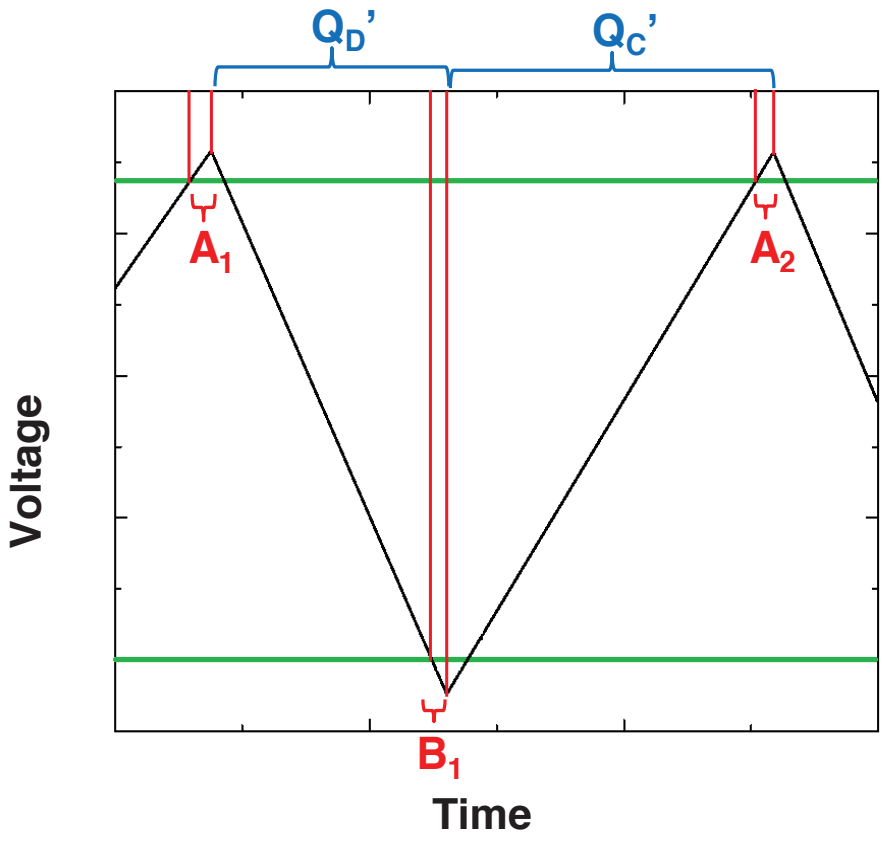

Figure 3.7 A diagrammatic illustration of how capacity is corrected for charge that is transferred beyond fixed voltage limits. Q_D' and Q_C' refer to the uncorrected charge and discharge capacities, respectively, that are integrated over the time intervals indicated. A_1, B_1, and A_2 refer to the amount of charge transferred over the indicated time (after exceeding a voltage limit).

Q_D' and Q_C' denote the uncorrected discharge and charge capacities, respectively. This would be the capacity calculated if measured voltage data were used directly (with no interpolation). Prior to Q_D', the cell is charged to a point that exceeds the upper voltage limit by some amount. The polarity of the current source is not switched until directly after this last voltage point is measured, so an amount of charge, denoted by A_1, is transferred to the negative electrode from the positive electrode between the time at which the voltage limit is crossed (determined by interpolation) and the time at which the current source is switched to discharge. Similarly, when the cell is discharged to the

lower voltage limit, the same situation occurs, and an amount of charge (denoted by B_1) is transferred to the positive electrode from the negative electrode. In order to determine the amount of charge that was transferred between endpoints, both of these excess amounts of charge must be subtracted from the discharge capacity. The same procedure is likewise performed on the subsequent charge capacity (Q_C') resulting in the following definition for the corrected discharge and charge capacities (Q_D and Q_C, respectively):

$$Q_D = Q'_D - A_1 - B_1 \qquad Q_C = Q'_C - B_1 - A_2 \qquad 3.2$$

This procedure was not applied to the HPC data shown in Figure 3.5. When data from the HPC is processed in this manner, a significant reduction in CE scatter is observed. Figure 3.8 shows data collected on the HPC that was processed with and without the correction procedure described above.

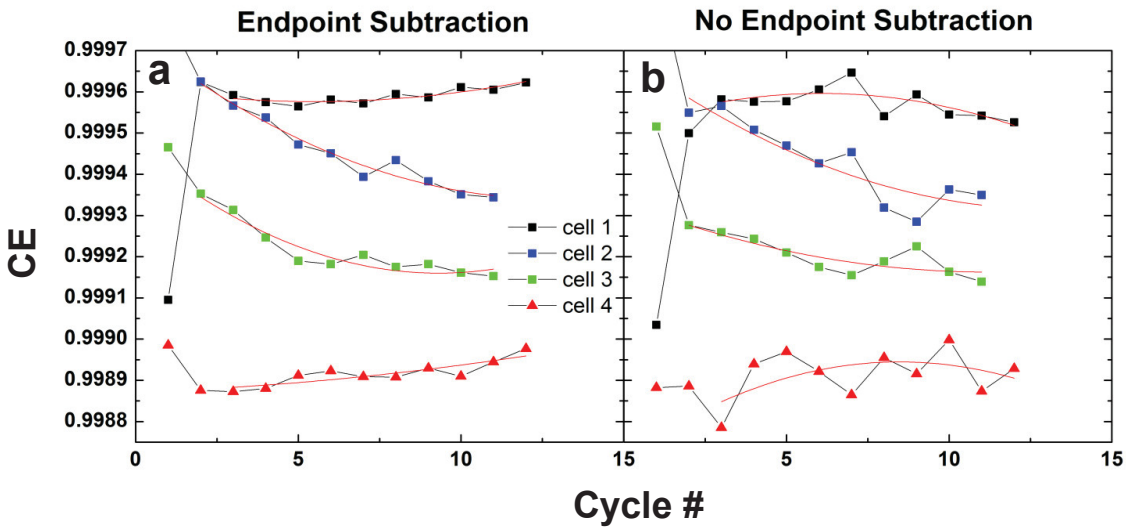

Figure 3.8 **a)** CE data collected on the HPC (from different LTO/LCO commercially manufactured cells) which was processed without subtracting excess charge from capacity. **b)** CE calculated from the same raw data as '**a**' with capacities corrected for excess charge.

Cell #	RMSE (with EP sub.)	RMSE (w/o EP sub.)
1	10 ppm	30 ppm
2	20 ppm	45 ppm
3	22 ppm	28 ppm
4	17 ppm	59 ppm
Average	**17.3 ppm**	**40.5 ppm**

Table 3.3 RMS error values of CE data shown in Figure 3.9.

Table 3.3 shows that the RMS error was reduced from an average of 40.5 ppm to an average of 17.3 when endpoint correction was used to calculate CE. This 17 ppm average can be regarded as the point of comparison for other CE data discussed in this thesis. All data presented in the remainder of this thesis is calculated using this charge correction procedure as described.

3.5 An Example of an Electrolyte Additive Study Using the HPC

In order to illustrate how the HPC is used and why increased precision in CE measurements is desirable, some results from a study [16] are presented here in which the effect of an electrolyte additive was analyzed using the HPC. The additive used was vinylene carbonate, (VC) which is widely studied and has previously shown increased capacity retention (especially at higher temperatures) when present in a variety of full and half cells . VC is generally added to an electrolyte mixture in small quantities, and is thought to improve capacity retention through the formation of a smoother, more stable SEI [15].

The purpose of the study discussed here was to investigate the effect of different concentrations of VC on the performance of full cells containing LCO and NMC ($Li[Ni_{0.42}Mn_{0.42}Co_{0.16}]O_2$) positive electrodes [16]. Commercially manufactured wound cells were provided by Medtronic Inc. which all contained MCMB (graphite) negative electrodes. Two separate sets of graphite/LCO cells were constructed with different ratios of positive and negative electrode masses, such that one of the sets could be charged to a higher voltage while maintaining the same maximum level of lithiation in the graphite electrode. The "high-voltage" set was cycled over the range of 3.4-4.175 V, while the "low-voltage" set was cycled over a range of 3.4-4.075 V. The graphite/NMC cells were cycled over a range of 3.3-4.225 V. Each of the 3 types of cells (high-voltage LCO, low-voltage LCO, and NMC) were made using an electrolyte solution composed of 1 M $LiPF_6$ dissolved in EC:EMC, (in a 3:7 volumetric ratio) and either 1% or 2% (by

weight) VC. A control set was also used, which contained no VC. Most of these cells were produced in pairs in order to demonstrate reproducibility.

All sets of cells were cycled on the HPC at a rate of C/20 in a temperature control box set to 40 ºC. The resulting normalized discharge capacity and CE data are shown in Figure 3.9.

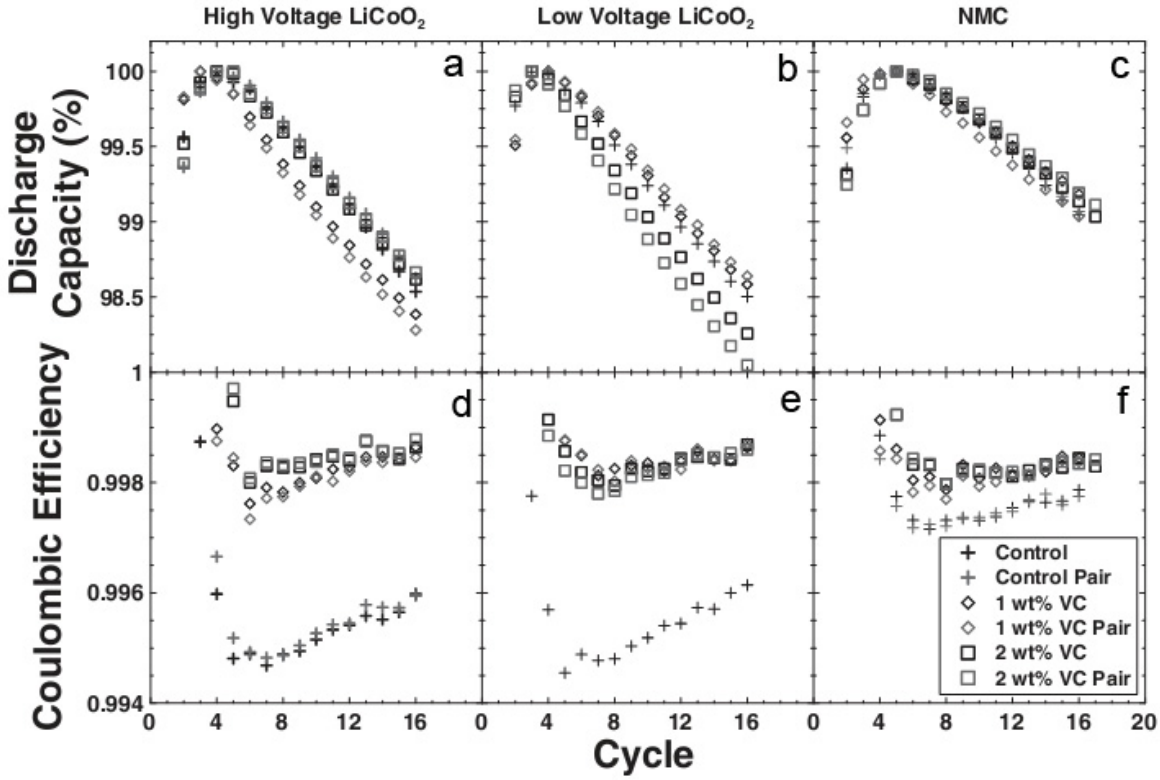

Figure 3.9 Normalized discharge capacity (**a**, **b**, **c**) and CE (**d**, **e**, **f**) of wound cells that were cycled on the HPC. Cells were composed of graphite negative electrodes and various positive electrodes as indicated. Cells were constructed using an electrolyte solution containing 0%, 1%, or 2% VC (by weight) [16].

Although there appears to be little noticeable effect of VC on capacity fade, (the slope of the normalized discharge capacity data) there is a significant difference in CE

compared to the control cells, especially for those cells containing LCO. However, the differences in CE between the cells containing 1% and 2% VC are much more difficult to resolve. For the low-voltage LCO data, it appears that the cell with 2% VC yielded a very slight increase in CE over the cell with 1% CE, but it is not at all clear which concentration of VC showed improved CE for the NMC or low-voltage LCO cells. In order to resolve any such potential differences, an increased level of precision is required.

3.6 Summary

This chapter serves as an overview of the theoretical and practical considerations involved in the design, construction, and operation of a high-precision charger system. The discussion focused on work previously done in the Dahn lab to build a charger system that exceeds the precision and accuracy of commercial charger systems currently available. The HPC at Dalhousie University was the state of the art at the beginning of this project and represents the starting point for all of the research presented in the subsequent chapters of this thesis. Chapter 4 will describe the design and construction of a new prototype charger system meant to improve upon the HPC described here.

CHAPTER 4 THE ULTRA HIGH-PRECISION CHARGER

The HPC system described in Chapter 3 serves as the starting point for the work presented in this thesis. The main objective at the outset of this project was to improve upon the performance of the HPC by making modifications to the basic design. To this end, a small-scale prototype charger system was constructed using the same current sources (Keithley 220s) and DMMs (Keithley 2000s) that were used to build the HPC. However, the design of this new charger system contained several fundamental modifications that were designed to improve the precision and accuracy of capacity and CE measurements. These modifications include:

- *In situ* measurement of current output that is used to calculate capacity
- Temperature control of current sources and DMMs
- Voltage stabilization of power supplied to current sources and DMMs
- Increased sample rate (for measuring both cell voltage and current)

The implementation of each of these modifications is described in detail in the following sections of this chapter.

For the sake of brevity, this new prototype system is referred to in this thesis as the Ultra High-Precision Charger (UHPC). The construction of the UHPC began near the end of 2010 and has progressed from a single-channel prototype to its current configuration of 3 channels (shown in Figure 4.3). This chapter describes the design and construction of the UHPC, as well as the preliminary results acquired from the system in

its initial single-channel configuration. The theory and implementation of the above-mentioned design modifications are discussed in detail.

4.1 *IN SITU* MEASUREMENT OF CURRENT

As previously mentioned, capacity is calculated by integrating current over the time it takes for a cell to be charged or discharged over a fixed voltage range. Many charger systems (including the HPC described in Chapter 3) achieve this by assuming the output of current sources to be a constant value (i.e. the set point that is entered into the current source). This makes the integration of current a simple matter of multiplying the constant value by the charge/discharge time interval:

$$Q = \int I(t)dt = I(\Delta t) \tag{4.1}$$

Calculating capacity in this manner can be a good approximation, provided that the output of the current source is stable, low-noise, and sufficiently accurate. Instead of relying on this assumption, the UHPC was designed to measure the current output versus time for every channel. Capacity was then calculated by numerically integrating the measured current data with respect to time.

The measurement of current was carried out using a second Keithley 2000 DMM to measure the voltage drop across a high-precision resistor (which was connected in

series between the cell and the current source). Figure 4.1 shows a schematic representation of this arrangement.

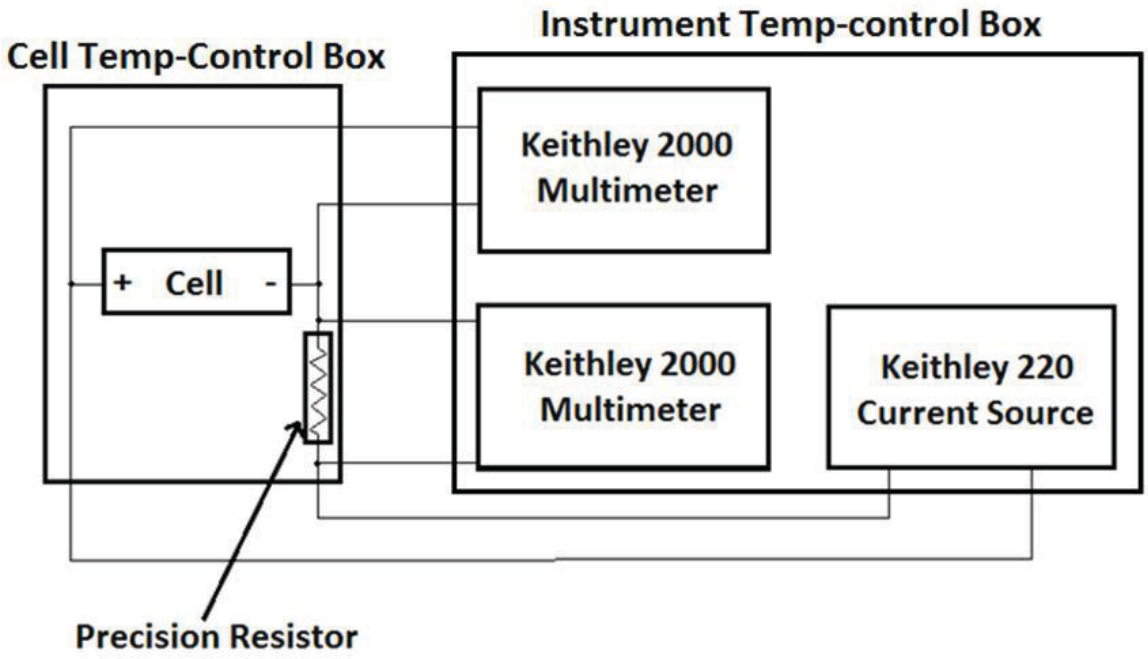

Figure 4.1 A schematic diagram of the UHPC showing how current measurement is implemented.

The instrument temperature control box shown in Figure 4.1 is discussed in the next section. The high-precision resistor was housed in the cell temperature control box so as to minimize any changes in resistance due to variation in temperature. The data sampling rates of the two Keithley 2000 DMMs were synchronized so that a single data point consists of a timestamp with an associated voltage and current value.

The high-precision resistor used for this purpose (a Z-foil™ series resistor purchased from Texas Components) was chosen for its high tolerance value, (0.005%) low noise, (0.01 μV per 1 V of applied potential) and low temperature coefficient (0.2 ppm/ºC). Separate sets of 6 resistors with resistance values of 1 Ω, 10 Ω, 100 Ω, 1 kΩ,

The cell temperature control box used the same basic "box within a box" design as those described in Chapter 3, but since the UHPC was only built up to 3 channels, the grid of sockets for cell holders that lines the back wall was omitted. A 60 mm fan and RTD are also used in the same fashion as described in Chapter 3.

4.2 Temperature Control of UHPC Instruments

The current sources and DMMs which comprise the UHPC utilize components (resistors, etc.) which are temperature-dependant. Reducing variation in the ambient temperature to which instruments are exposed may thus result in improved performance. In order to limit the temperature variation of these instruments, a Yamato D600 oven with high-precision temperature control was modified for this purpose. Figure 4.3 shows the UHPC (excluding the cell box) in its final 3-channel configuration.

Figure 4.3 The modified temperature control box used to house current sources and DMMs of the UHPC

10 kΩ, and 100 kΩ were purchased for each channel. Resistance values were chosen for each experiment such that the voltage drop across the resistor was within the range of 1-10 V, given the applied current. This was done because the Keithley 2000 measuring the voltage drop across the resistor performs best in that range (specifically, the temperature coefficient of the Keithley 2000 is lowest in this range). In order to further minimize temperature variation of the resistor, aluminum heat sinks were constructed using blocks of aluminum with holes into which the resistors were inserted. Figure 4.2 shows an example of one of the resistors and an aluminum block used, and demonstrates how they were arranged in the cell temperature control box.

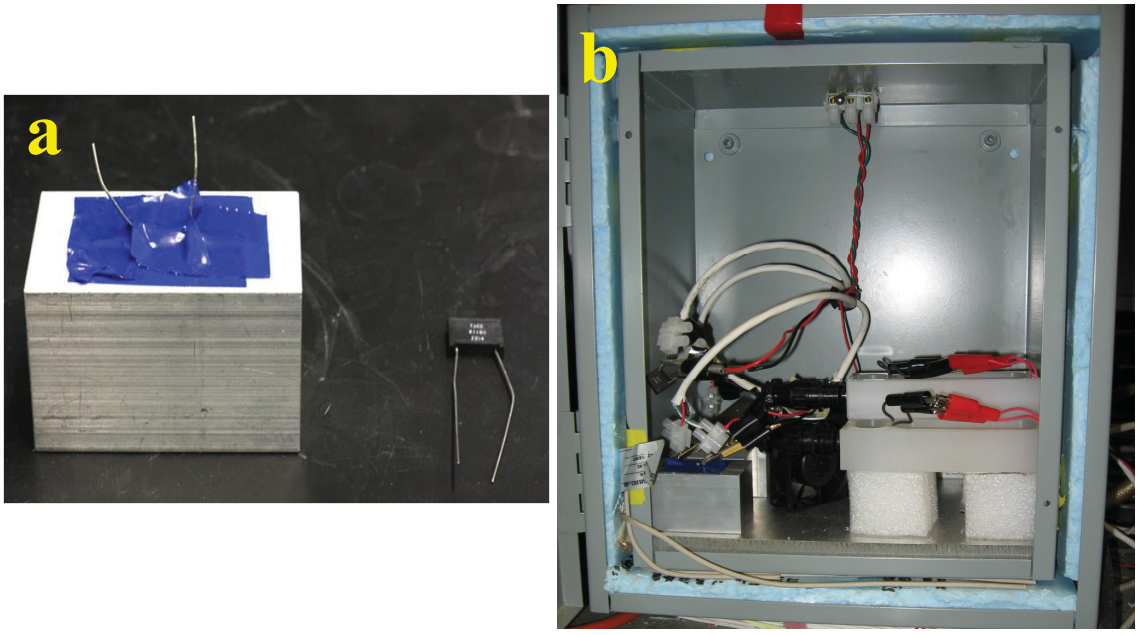

Figure 4.2 **a)** One of the high-precision resistors used (right) and the aluminum block used as a heat sink (left) with resistor inserted. **b)** Inside of the UHPC cell temperature control box. Resistors in heat sinks are on the bottom left, cell holders are on the right.

It was hoped initially that the oven could be used as-is to control instrument temperature, but heat generated by the current sources was significant enough to exceed the maximum operating temperature (35 º C) of the instruments when enclosed in the oven. In order to overcome this problem, the oven was modified to include a heat management apparatus and an air intake cooling system. In order to manage the heat produced by the current sources, a hole was cut into roof of the oven into which a high-flow, 120 mm server cabinet fan was installed. The fans on the rear panels of each current source were reversed so that hot air was expelled from the instrument. An aluminum manifold was then constructed which shuttled this hot air directly to the 120 mm exhaust fan. Figure 4.4 shows a schematic of this system.

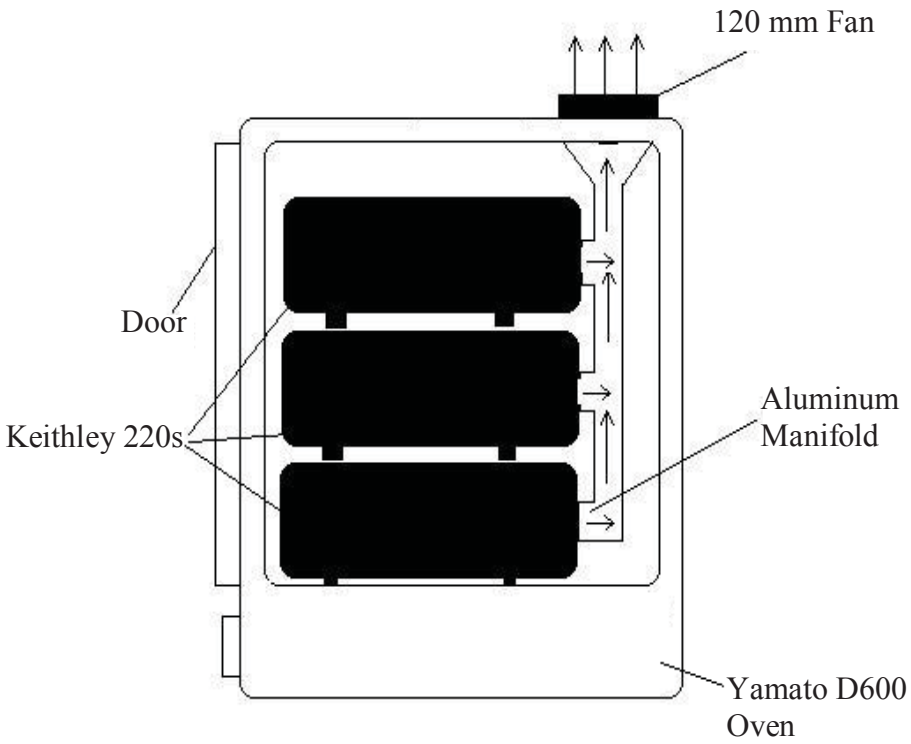

Figure 4.4 A schematic diagram of the system used to manage heat produced by current sources.

Since this heat management system required the removal of hot air from the oven, room-temperature air was sucked into the oven through a hole on the right-hand wall. Using room temperature air was not itself sufficient to reduce the operating temperature in the oven to below 35 ºC, and it was also found to increase the variation in oven air temperature. To counteract this, an intake cooling system was constructed so that air coming into the oven was both cooler and of less variable temperature. Figure 4.5 shows the intake cooling system as constructed.

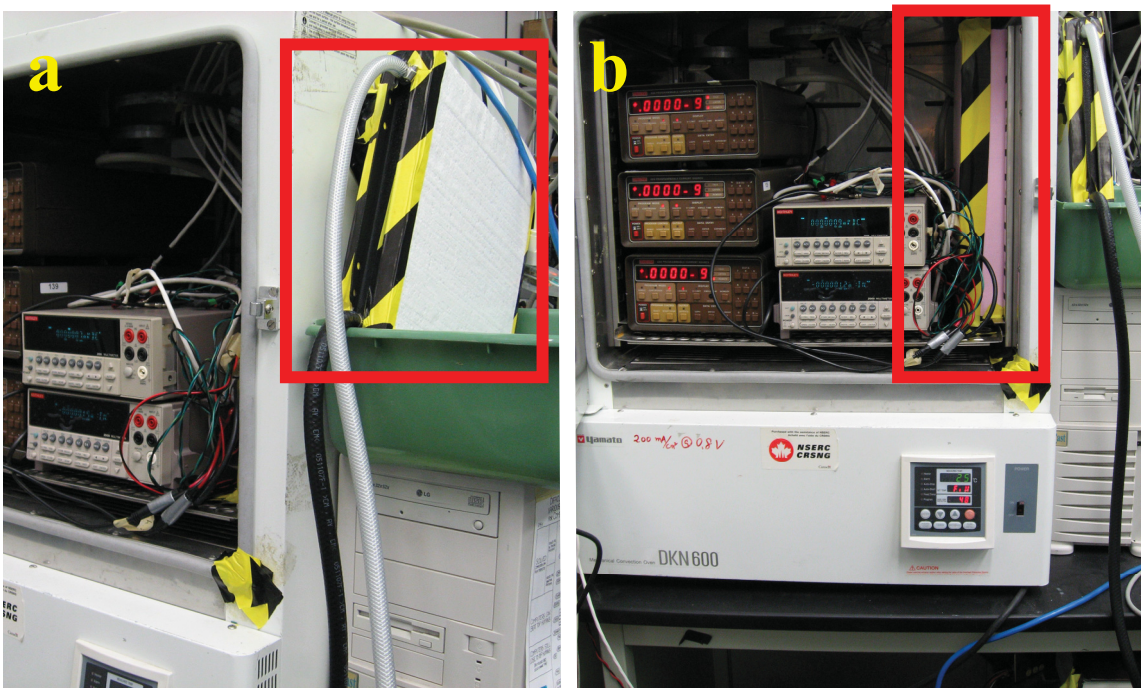

Figure 4.5 **a)** Insulated radiator (highlighted) used for cooling oven air intake (hoses connect to cooling unit - not pictured). **b)** Insulated manifold (highlighted) for delivering cooled air to the oven's internal circulation fan.

The insulated box pictured in the inset of Figure 4.5-a housed a car radiator that was connected to an external liquid cooling unit (using ethylene glycol as the coolant). This box was sealed on all sides except the bottom edge, (obscured in this picture) where

room-temperature air can pass into the box and over the radiator where it was cooled. The cooled air then passed from the radiator box, through an air intake hole in the side of the oven, then into an insulated manifold (shown in Figure 4.5-b). The purpose of this manifold was to deliver the cooled air directly to the bottom of the oven, where the internal circulation fan of the oven was located. The cooled air is then mixed with the air in the oven inside a compartment beneath the instrument rack before being circulated. The use of this manifold prevented the development of a temperature gradient that would otherwise result from applying cooled intake air directly to the DMMs which reside on the right side of the oven, next to the cold air intake.

The temperature of the coolant fluid used in the radiator was optimized such that the operating temperature variation in the oven was smallest. The optimal coolant temperature was found to be 7 ºC in this situation. The temperature control system operated by constantly cooling the instruments, while simultaneously using the heating controller in the oven to monitor and control the temperature. While not particularly energy efficient, this system performed very well in terms of limiting temperature variation. Figure 4.6 shows the ambient temperature variation inside the oven (compared to room temperature and cell box temperature).

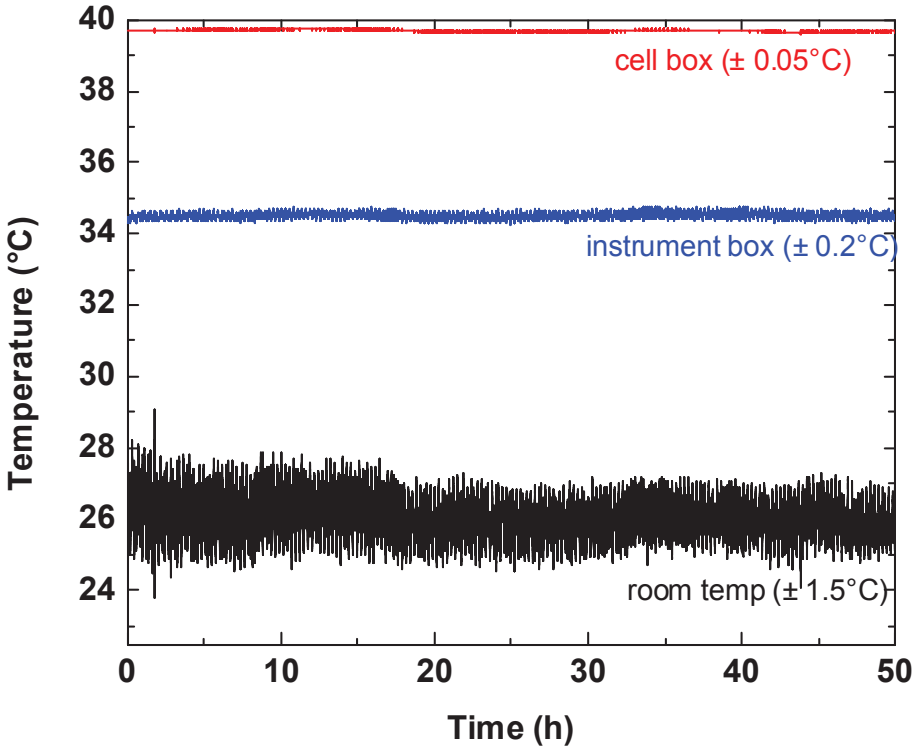

Figure 4.6 Temperature data from the cell box and instrument box (modified oven) of the UHPC as compared to the room temperature in the lab where the HPC and UHPC are housed.

This data shows that the resulting temperature variations in the modified oven were almost an order of magnitude less than the room temperature variation in the lab containing the HPC and UHPC (which is itself temperature-controlled by an air conditioning unit). The instrument temperature control is not quite as good as the temperature control in the cell box, but it is sufficient to determine whether it yields a performance enhancement over instruments exposed to the much larger room temperature variation.

4.3 Voltage Stabilization and Sample Rate

Fluctuations in the AC voltage of municipal power grids are common, as demand placed on the grid increases during the day and decreases at night. In order to limit these variations in the electricity used to supply the UHPC's current sources and DMMs, a voltage stabilizer from Ashley-Edison was used to constrain voltage output to within ±1%. Figure 4.7 shows the daily variation in voltage from a wall socket connected to the Nova Scotia Power grid, as well as the output of the voltage stabilizer.

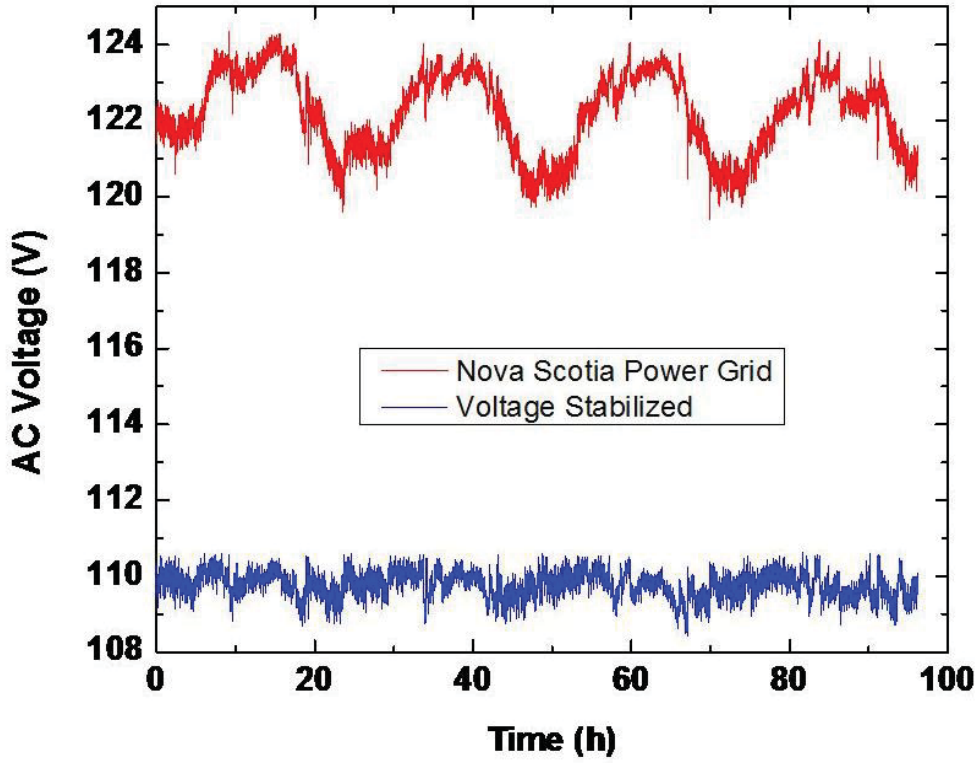

Figure 4.7 The output of a voltage stabilizer compared to the unstabilized voltage measured directly from the Nova Scotia Power grid.

In addition to the hardware modifications previously mentioned, the sample rate of the UHPC was also greater than that of the existing HPC. In Chapter 3, it was mentioned that the HPC dwells on each channel for 500 ms before taking a voltage reading. This is also done with the UHPC, but instead of scanning over a system of 10 channels (resulting in a 5- to 6-second delay) the UHPC was built up to a maximum of 3 channels (resulting in a 1.5- to 1.7-second delay). Although CE data from the HPC was calculated using the endpoint interpolation procedure described in Chapter 3, a greater sample rate may still yield an improvement in performance.

4.4 Preliminary Results

The UHPC was first assembled as described in a 1-channel configuration for preliminary testing. The software used to control the UHPC is a modified version of the Labview program used to control the existing HPC. The first test performed on the UHPC used a LTO/LCO commercially manufactured cell. The cell was cycled at a rate of C/10 between 1.8 V and 2.8 V, and was held at a temperature of 30 ºC. For all experiments performed on the UHPC, it was possible to calculate capacity and CE by either integrating the measured current data, or by ignoring the current data and using the assumption of constant current output (as is done with the existing HPC). The measured and constant current CE data from this first experiment is shown in Figure 4.8.

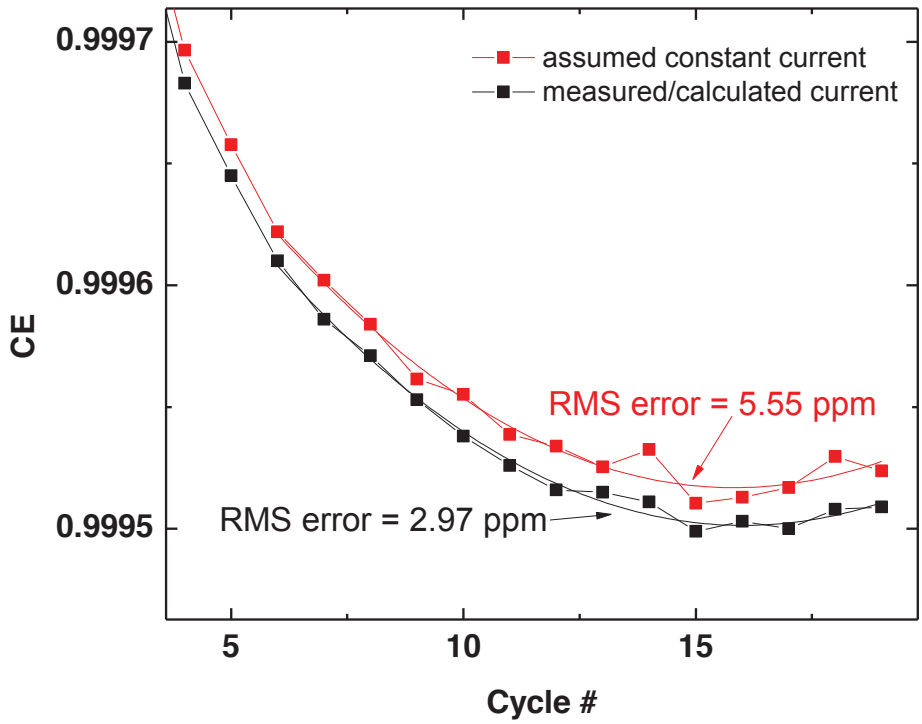

Figure 4.8 CE data from the first experiment performed on the UHPC (using a commercial LTO/LCO cell run at C/10 at 30 ºC).

The results of this experiment were very promising, as the scatter of the measured current data was several times lower than the 10-20 ppm range of the existing HPC. This experiment also indicated that the CE data calculated using constant current contains not only more scatter, but is also shifted with respect to the measured current data. This shift in CE can arise if there is an imbalance in the magnitude of charge and discharge currents, which would in turn affect the ratio of charge and discharge capacities. Since using constant current assumes that the magnitudes of these currents are exactly equal, it can lead to inaccuracy in CE data. The current source used here was calibrated immediately before the experiment was carried out, so this data indicates that measuring

current leads to improved accuracy, even if proper calibration is performed. The CE data shown here is above 99.95%, which would be close enough to unity (1.0000…) to make precise measurement with many commercial chargers difficult (which, as described in Chapter 3, often yield CE scatter on the order of ±0.5%).

The low level of CE scatter demonstrated in Figure 4.8 has been reproducible throughout the duration of this project. Table 4.1 shows the results of all experiments conducted with all of the aforementioned modifications in place.

Experiment	RMS Error (ppm)
First Cell	2.97
TB1026A	2.66
TB1026B	3.52
TB1027A	4.65
TB1027B	3.66
TB1032A	4.86
TB1032B	9.99
TB1032C	6.86
TB1038A	5.82
TB1038B	2.72
Average	**4.77**

Table 4.1 RMS error of CE data from all experiments performed on the UHPC with all modifications in place as described. The left column contains reference codes used to identify experiments.

Table 4.1 shows that the UHPC can reproducibly yield CE scatter with RMS error that is below 5 ppm. The result of one experiment yielded an RMSE of 9.99 ppm, which is unusually high, but a Q-test determined that this value is not a statistical outlier (with a confidence of 95%).

When the UHPC was built up to its present 3-channel configuration, an experiment was carried out to evaluate channel-to-channel variation. Three newly-manufactured "identical" commercial graphite/LCO with were cycled at a rate of C/10 using a cell temperature of 30ºC. Figure 4.9 shows the results of this experiment.

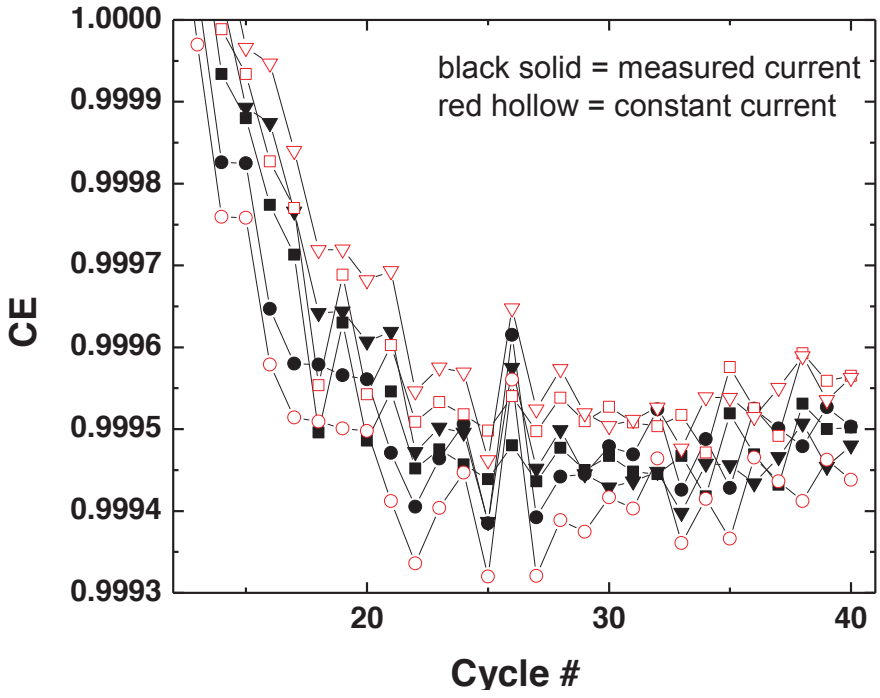

Figure 4.9 CE data from 3 graphite/LCO cells that was calculated using measured and constant current.

There is a visible improvement in channel-to-channel variation when measured current is used instead of constant current. A spike in CE at cycle 26 was due to a malfunction in the lab air conditioning system which caused cell temperature to temporarily rise above 30ºC, so the polynomial fits used to calculate channel-to-channel variation were performed on data from cycles 27 through 40. The resulting channel-to-channel variation was 124 ppm for the constant-current data and 33.2 ppm for the measured-current data.

Although the UHPC performed well, it remained to be seen exactly how each of the described modifications contributed to the observed reduction in CE scatter. This is important, as it would provide a set of design principles upon which to build future high-precision charger systems and/or modify the existing HPC. This information would also be very useful to other researchers and charger manufacturers wishing to develop a similar system.

4.5 Summary

The UHPC was built using the same basic design principles as the HPC that preceded it. Through the use of measured current, temperature control of instruments, stabilization of voltage supplied to instruments, and increased sample rate, a significant and reproducible reduction in CE scatter was demonstrated (with RMS error less than 5 ppm). The remainder of this thesis focuses mainly on determining the contribution of each hardware modification to this observed reduction in CE scatter. Other advantages of the UHPC, such as improved accuracy and the ability to perform experiments with variable current output, are also discussed.

CHAPTER 5 A DETAILED ANALYSIS OF THE UHPC

Following the design and construction of the UHPC, initial results demonstrated a significant reduction in CE scatter as outlined in the preceding chapter. However, since these results were achieved with all of the previously described modifications in place, (i.e. measured current, temperature control of instruments, voltage stabilization, and increased sample rate) the respective contribution of each modification to this improved precision was not clear. A more detailed investigation of each modification was necessary in order to make recommendations for the design of future high-precision charger systems.

This chapter provides a quantitative analysis of each modification. Separate sets of experiments were carried out to isolate the effects of instrument temperature control and voltage stabilization, as well as to investigate the effect of increased data sample rate. As previously mentioned, both measured and constant current can be used to calculate results for every experiment, so the effect of using measured current is discussed in detail throughout the presentation of these results.

In addition to these experiments, some preliminary work on 2-stage charging is presented (which is described in detail in Section 5.3). The performance of the UHPC is also compared to a commercial prototype for a "high-precision add-on" provided to us by A and D Technologies, as well as a Maccor Series 4000 charger system.

5.1 Instrument Temperature Control and Voltage Stabilization

In order to isolate the contribution of instrument temperature control and voltage stabilization to the observed drop in CE scatter, a set of experiments were carried out where the UHPC was run using different configurations as follows (in chronological order):

- Both temperature control and voltage stabilization in place
- Temperature control, but no voltage stabilization
- Voltage stabilization, but no temperature control
- No voltage stabilization or temperature control

At the time this experiment was performed, the UHPC was running in a 2-channel configuration. The cells used for these experiments were 2 commercially manufactured LTO/LCO cells from Medtronic Inc. which contained the electrolyte additives, VC and trimethoxyboroxine (TMOBX). These cells had been previously used for different experiments and were not expected to yield exactly the same CE (i.e. their results are not intended to demonstrate channel-to-channel noise). The cells were run at a rate of C/10 at a temperature of 30 ºC over a voltage range of 1.8-2.8 V. Figure 5.1 shows the CE data from these experiments in chronological order.

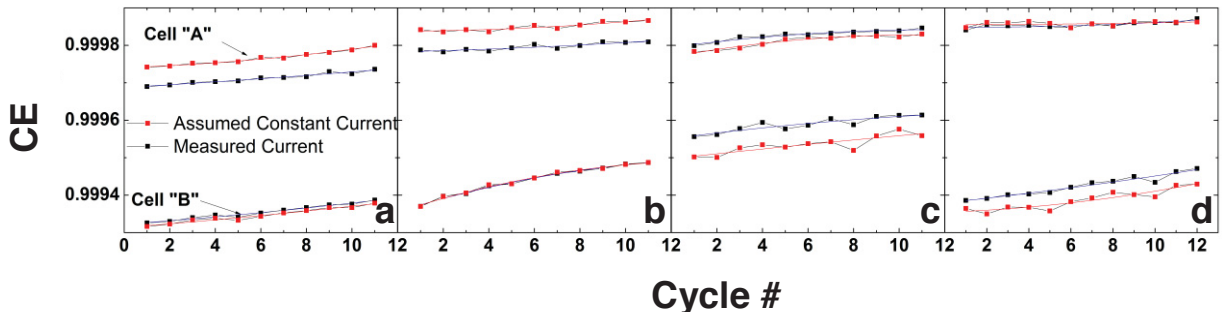

Figure 5.1 CE data from the UHPC (in chronological order) run in the following configurations: a) Temperature control and voltage stabilization in place b) No voltage control c) No temperature control d) No temperature control or voltage stabilization.

This data shows a smooth increase in CE from experiment to experiment, with the exception of the last experiment, which shows a drop in the CE of cell B (the cause of this drop is unknown). This steady increase in CE is common behavior for Li-ion cells, as the rate of SEI formation slows over time, resulting in reduced parasitic current. The CE data from experiments conducted without temperature control of instruments (panels c and d) are visibly noisier than the data collected with temperature control (panels a and b). The actual RMS error values for each of these experiments are shown later in Figure 5.3.

In Figure 5.1, the constant current data of both cells shows a significant downward shift (with respect to the measured current data) when temperature control of the instruments was removed. The temperature inside the oven was approximately 8 ºC hotter than the surrounding room temperature, (see Figure 4.6) which would certainly be a large enough difference to significantly affect the output of the current source. If the change in the magnitude of the current source output were the same for the charge and discharge currents, then no shift in CE would be expected. The data in Figure 5.1

indicates that the charge and discharge currents are indeed affected differently by changes in temperature. This is supported by raw current data, shown in Figure 5.2.

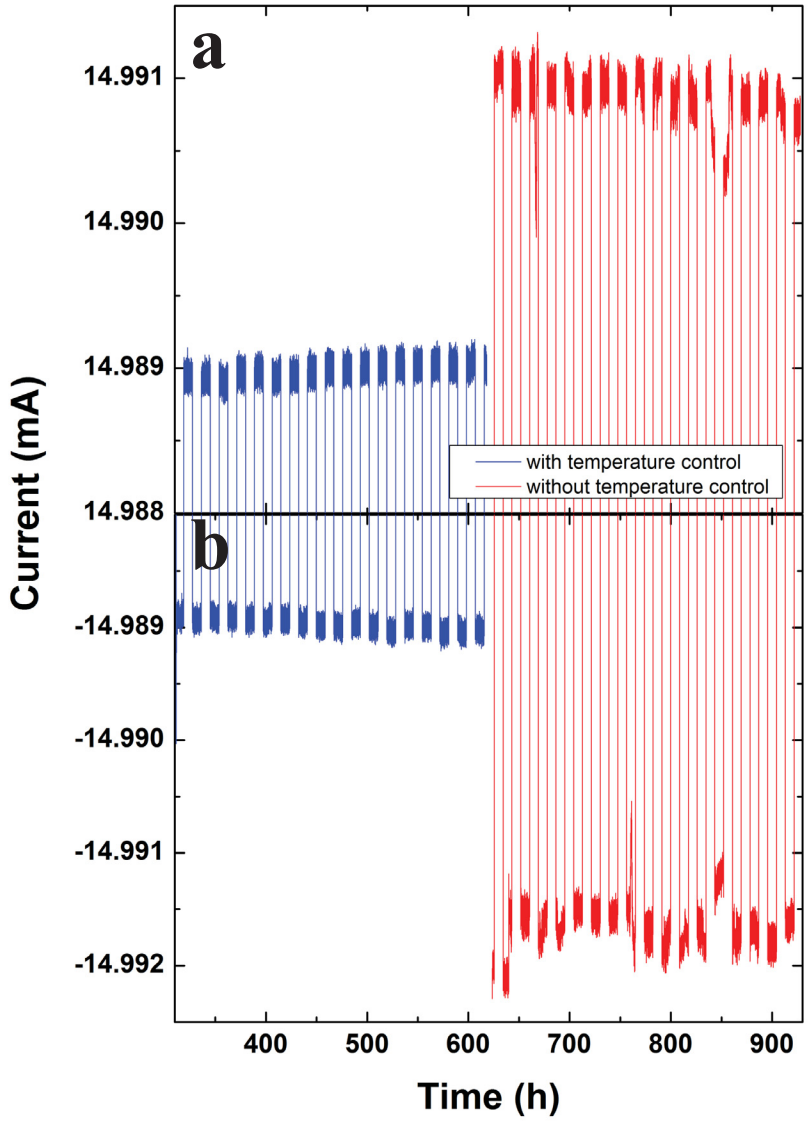

Figure 5.2 **a)** Charge and **b)** discharge current with and without temperature control of instruments. This current corresponds to the data shown for cell B in panels **b** and **c** of Figure 5.1.

Figure 5.2 shows that the charge and discharge current output did indeed react differently to the drop in temperature. The charge current output jumped by ≈ 2 μA, while the

magnitude of the discharge current jumped by ≈ 3 μA. The Keithley 220 modules used are actually composed of 2 separate internal current sources, (one for charge and one for discharge) so the observed change in charge/discharge balance are likely due to a slight difference in the temperature coefficient of each internal source.

In addition to the observed shifts in current output, the CE scatter of the measured current data in Figure 5.2 also became significantly greater temperature control was removed. This increase is much greater for cell B than for cell A. The current output of the channel used to cycle cell B was considerably noisier than that of the channel used to cycle cell A, which is the likely cause for this increase. Since this data was acquired by a DMM that was also exposed to room-temperature air, it is possible that the observed variation in current could be due to measurement error of the DMM, rather than an actual change in current source output. This is unlikely however, as the rated temperature coefficient of the current source is much higher (≈100 ppm/ºC) than that of the DMM (≈3 ppm/ºC) in the ranges used here. The high-precision resistors that were used to measure current remained under temperature control in the cell box, and would not have contributed further to current measurement error. The scatter of measured- and constant-current CE data (discussed below) also supports the assertation that the observed variation in current is chiefly due to actual changes in source output.

The effects of temperature control, voltage stabilization, and measured current are summarized in Figure 5.3, which shows the averaged RMS error of both cells, calculated for each experiment using both measured and constant current.

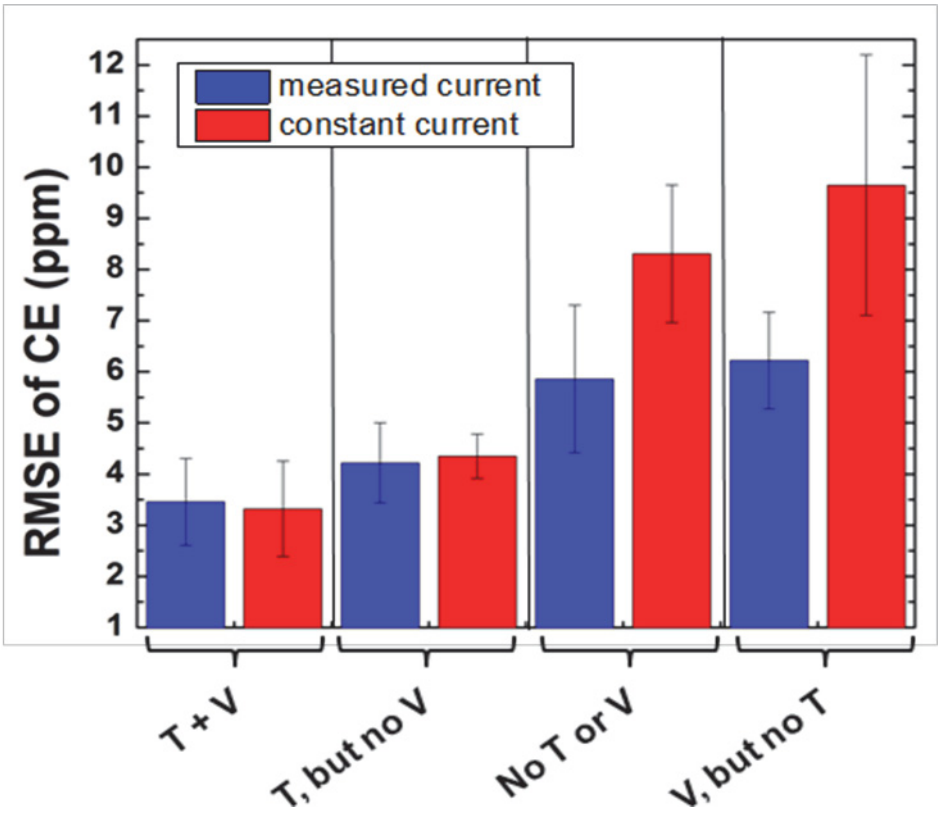

Figure 5.3 RMS error, averaged from cells "A" and "B," for each of the 4 experiments performed on the UHPC using the configuration indicated. For the x-axis labels, "T" refers to instrument temperature control and "V" refers to voltage stabilization. Error bars indicate one standard deviation.

There are several important conclusions that can be drawn from Figure 5.3. The first 2 sets of columns in Figure 5.3 show no significant difference in CE scatter for the data collected with and without voltage stabilization. The right-hand 2 sets of columns also show no improvement for the voltage-stabilized data (when temperature control was not in place). The voltage stabilizer thus did not appear to have any discernible effect on CE precision. Comparison of the results calculated using measured current compared to those calculated using constant current shows that there was no change in CE scatter when the instruments were under temperature control. However, the constant-current data was significantly noisier than the measured-current data when temperature control

was removed. This is consistent with the current data shown in Figure 5.2, where the current output went from being stable and low-noise (when sources were temperature-controlled) to being unstable and noisy (when temperature control was removed). The assumption of constant current appears to be a good approximation as long as the sources are under temperature control, but the current output becomes noisier when the sources are exposed to room-temperature air, resulting in increased CE scatter. The use of measured current can correct for these variations, offsetting the increased CE scatter that results from variation of instrument temperature.

These experiments demonstrate that the use of measured current is an effective means of both reducing scatter, (in the absence of temperature-controlled instruments) as well as improving accuracy of CE measurements. Although the best results (< 5 ppm) were only achieved with temperature control of instruments in place, the use of measured current alone resulted in performance that was similar, but still significantly different (with a confidence of 95%) . The largest RMS error shown in Figure 5.3 is just under 9 ppm, which is still smaller than the scatter measured using the existing HPC (which yielded an average RMSE of 17 ppm, as discussed in Chapter 3). However, the UHPC collects data at a faster rate than the existing HPC, which may account for this discrepancy in CE scatter. The effect of data sample rate is analyzed in detail in the next section.

5.2 DATA SAMPLE RATE

Two separate situations must be considered when investigating the effect of data sample rate on CE precision: the measurement of current (which is important between charge/discharge endpoints) and the accurate determination of voltage limit intercepts (which takes place at the charge/discharge endpoints). The first situation was investigated by measuring and recording data at the highest possible sample rate and "thinning out" the acquired data using software post-processing (effectively lowering the sample rate between endpoints). The latter situation was investigated by running an experiment where the actual sample rate of the UHPC was lowered by increasing the delay period used between measurements of each channel. The results of these investigations are discussed separately.

5.2.1 Sample Rate of Current Measurement

As shown in Figure 5.2, the current source output became visibly noisier when temperature control was removed, making the assumption of constant current a less accurate approximation. In order to obtain a reduction in CE scatter as seen in Figure 5.3, the sample rate of current measurement must be high enough to accurately capture variations in current source output. The results shown in Figure 5.3 were obtained using the fastest possible sample rate, but the use of such a high sample rate on a large scale can be impractical (the size of the raw data files from these experiments were on the order of 150 MB per experiment, per channel).

In order to examine the effect of reduced sample rate of current measurements, raw data files (with current, voltage, and time data) were "thinned out" using software that was written for this purpose. This software operated by reading a raw data file, then producing a new copy of that file that was reduced in size by a given factor. For example, if a file were reduced by a factor of 3, the software would scan through the original data file and would only write every 3rd data point to the output file. In order to properly carry out interpolation of voltage endpoints, the last data point of every charge/discharge was always retained, as well as the data point immediately preceding it. The "thinned" output files were then used to calculate CE with the thinned-out current data. This procedure was performed on the raw data from one of the experiments discussed in Section 5.1 (specifically, the data from cell "B" shown in Figure 5.1, panel d). This data was used, as it showed the largest amount of current source noise. The maximum sample rate of this data was 1 point per 1.2 seconds. The resulting CE data is shown in Figure 5.4.

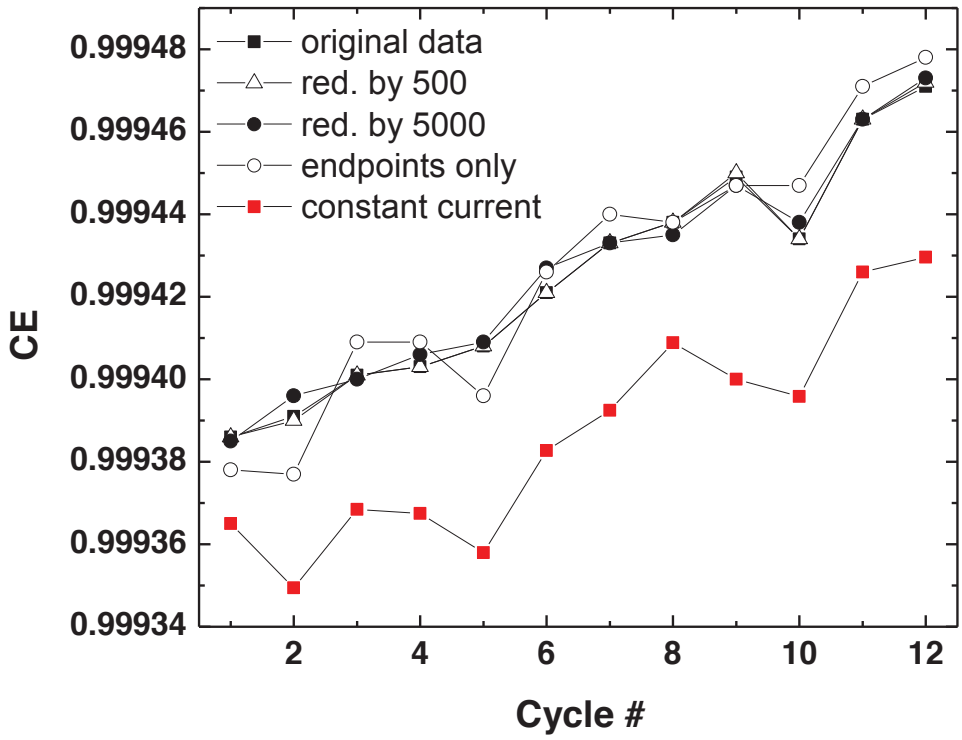

Figure 5.4 CE results which were obtained using current data that was reduced by different factors, as indicated. The term "endpoints only" refers to data that used only 2 data points for each charge/discharge (directly before and after crossing a voltage limit). The constant current data is also provided for comparison.

There is very little difference in Figure 5.4 between the results obtained using the original raw data and those using data that was reduced by a factor of 500. However, as the current data was further reduced, the CE scatter increased visibly, especially for the data which used only the endpoints of each charge/discharge. Although the scatter increased significantly as the files were thinned out, the CE data did not shift as was seen with the constant current data. This indicates that the imbalance between charge and discharge currents can still be accurately captured by measuring current once per cycle. The effective reduction in current measurement sample rate resulted in a decrease in CE precision, but no significant loss in accuracy.

In order to more precisely determine the point at which the reduction in current data begins to affect CE scatter, the above data was reduced by many different factors, and the RMS error of the resulting CE was calculated for each reduced dataset. The results of this procedure are shown in Figure 5.5.

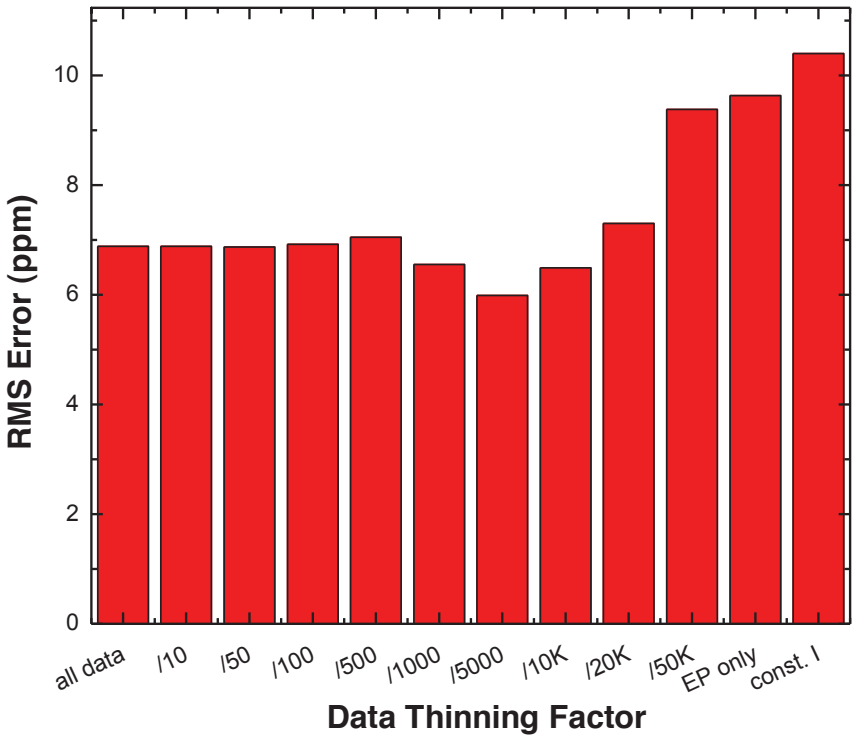

Figure 5.5 RMS error values for CE results calculated using current data that was reduced by the factors indicated on the horizontal axis. "EP only" refers to the use of only endpoint data, and "const I." refers to constant current (for comparison). This error does not capture the shift of the constant current data shown in Figure 5.4.

Figure 5.5 shows that there was essentially no change in CE scatter until the current data was reduced by a factor of 500. After this point, as the current data was further reduced, CE scatter actually decreased before increasing again to a maximum of just under 10 ppm (comparable to the scatter obtained using constant-current calculations). Since the

current data used for this experiment was relatively noisy, the process of thinning out this data can produce widely varying results (which provides a possible explanation for the drop in CE scatter when the data is thinned by a factor of 1000). Figure 5.6 shows an example of how different the current profile can become when reduced by a large factor.

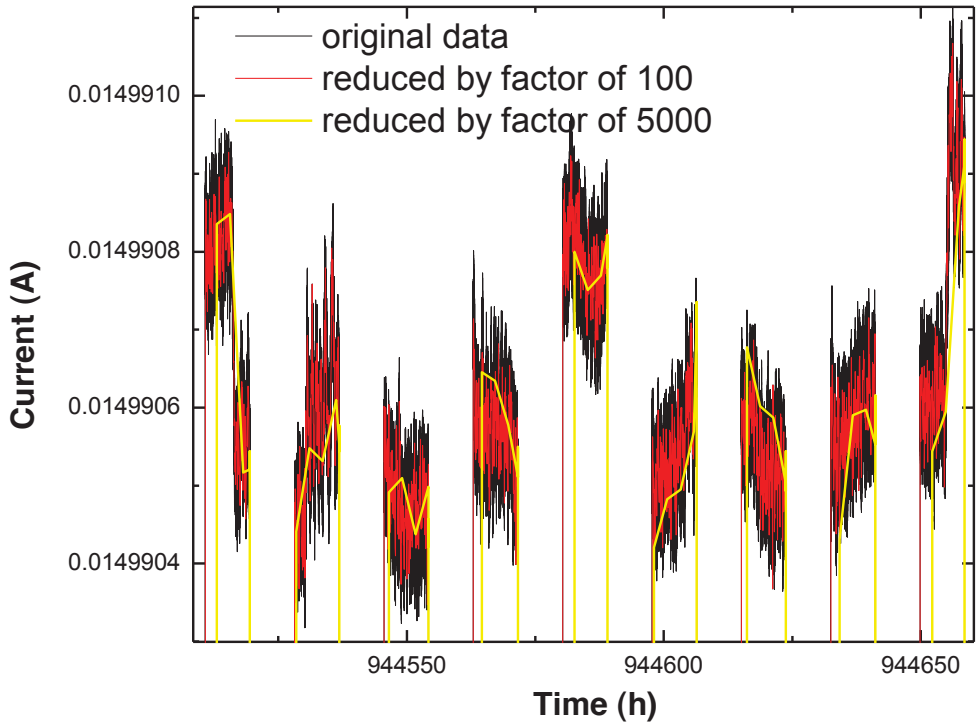

Figure 5.6 Charge current data from the experiment described above. The same data that has been reduced by factors of 100 and 5000 (respectively) are also shown.

Figure 5.6 shows that the data which was reduced by a factor of 100 is a relatively accurate representation of the original data (which is confirmed by the unchanged RMS error in Figure 5.5). However, the data that was thinned by a factor of 5000 does not accurately capture the current variation of the original data. The resulting CE data would

be expected to vary in a similarly random fashion, which could result in the non-uniform increase in RMS error that is shown in Figure 5.5.

The practical goal of this procedure was to determine a minimum sample rate that could be used to measure current without compromising CE precision. Any change in the level of CE scatter (positive or negative) indicated that variations in current were no longer being accurately captured, so this limit was determined using the data that was reduced by the largest factor without showing any impact on CE scatter. The data that was reduced by a factor of 100 meets this description, (as it yielded an RMSE that was the same as that of the original data to within 0.01 ppm) which corresponds to an effective sample rate of approximately 1 point per 120 seconds (2 minutes). This can be used as a general guideline for the operation of similar charger systems using a similar current output.

5.2.2 Sample Rate and Voltage Limit Overshoot

As described in Chapter 2, cells are always charged/discharged to a voltage that exceeds preset voltage limits. The slower the sample rate, the greater the variation in the degree of this voltage limit overshoot. For example, the HPC measures voltage data at a rate of approximately 1 point per 6 seconds, so a cell could be charged/discharged past a voltage limit by a time interval anywhere between zero and six seconds. Although endpoint interpolation is used to correct for this, a faster sample rate would reduce the variation in voltage overshoot, and may lead to increased precision.

In order to investigate the effect of sample rate on voltage limit overshoot, a post-processing approach as described in the previous section could not be used. Instead, an experiment was carried out where a set of 3 commercial cells were cycled on the UHPC using 2 different sample rates. The first experiment used the fastest possible sample rate (1 point per 1.7 seconds) and the sample rate of the second experiment was slowed to a sample rate of 1 point per 6 seconds (in order to simulate the sample rate of the existing HPC). This delay was programmed into the software, forcing the Keithley 2000 DMMs to wait for 2 seconds between measuring voltage and current of each channel (resulting in a total delay of 6 seconds to scan over all 3 channels). The aforementioned endpoint interpolation procedure was used to calculate the results of both these experiments. Figure 5.7 shows the resulting CE data obtained using both sample rates. The RMS error values obtained from this data is shown in Table 5.1.

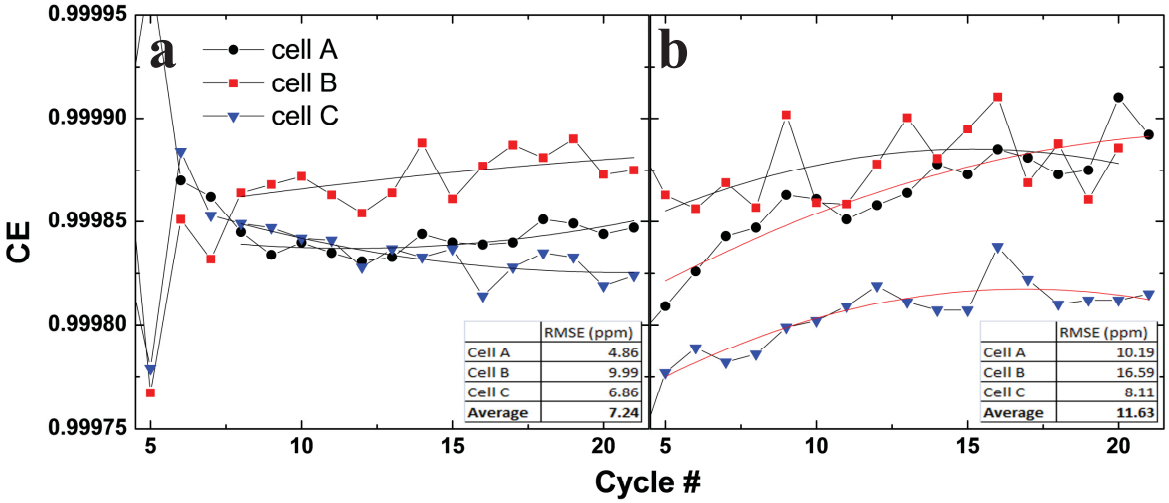

Figure 5.7 CE data collected from 3 Medtronic LTO/LCO commercial cells using a data sample rate of **a)** 1 point per 1.5 seconds and **b)** 1 point per 6 seconds. Cells were cycled at C/10 at 30 ºC.

This data shows a significant increase in CE scatter for all 3 cells tested, going from an average RMS error of 7 ± 3 ppm to 12 ± 4 ppm (a difference which is statistically significant with a confidence of 85%). The above errors correspond to one standard deviation. These results indicate that even with the use of endpoint correction as described, reducing the period between measurements from 6 seconds to 1.5 seconds yields an improvement in CE precision. These results can also be used to quantify channel-to-channel variation (which also includes cell-to-cell variation).

A more detailed analysis of the data shown in Figure 5.7-b indicated that the endpoint interpolation procedure actually appeared to be overcorrecting for voltage limit overshoot. This became apparent when CE from the low-sample-rate results (Figure 5.7-b) was compared with the same data that was calculated without the subtraction of excess charge that is transferred after crossing a given voltage limit. One of these comparisons is shown in Figure 5.8.

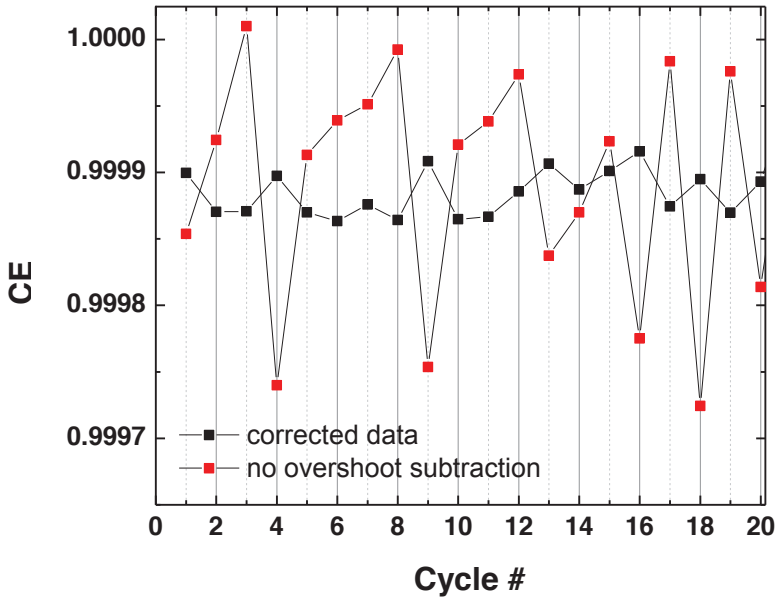

Figure 5.8 CE data from the same experiment as shown in Figure 5.7 b for cell "B," calculated with and without the subtraction of excess charge that is transferred beyond fixed voltage limits.

This data clearly shows that the subtraction of excess charge greatly reduces the amount of CE scatter, as expected. However, it also shows that the large spikes seen in the uncorrected data became inverted when endpoint correction was applied (for example, a sharp drop in uncorrected CE became a smaller upward jump in the corrected CE data). These spikes in CE are the result of spikes in charge and discharge capacity data, which in turn were found to strongly correlate to the degree of voltage limit overshoot. Figure 5.9 shows the amount of voltage limit overshoot at the charge and discharge endpoints for each cycle, as well as the corresponding capacity data (the uncorrected capacity data is also shown for comparison).

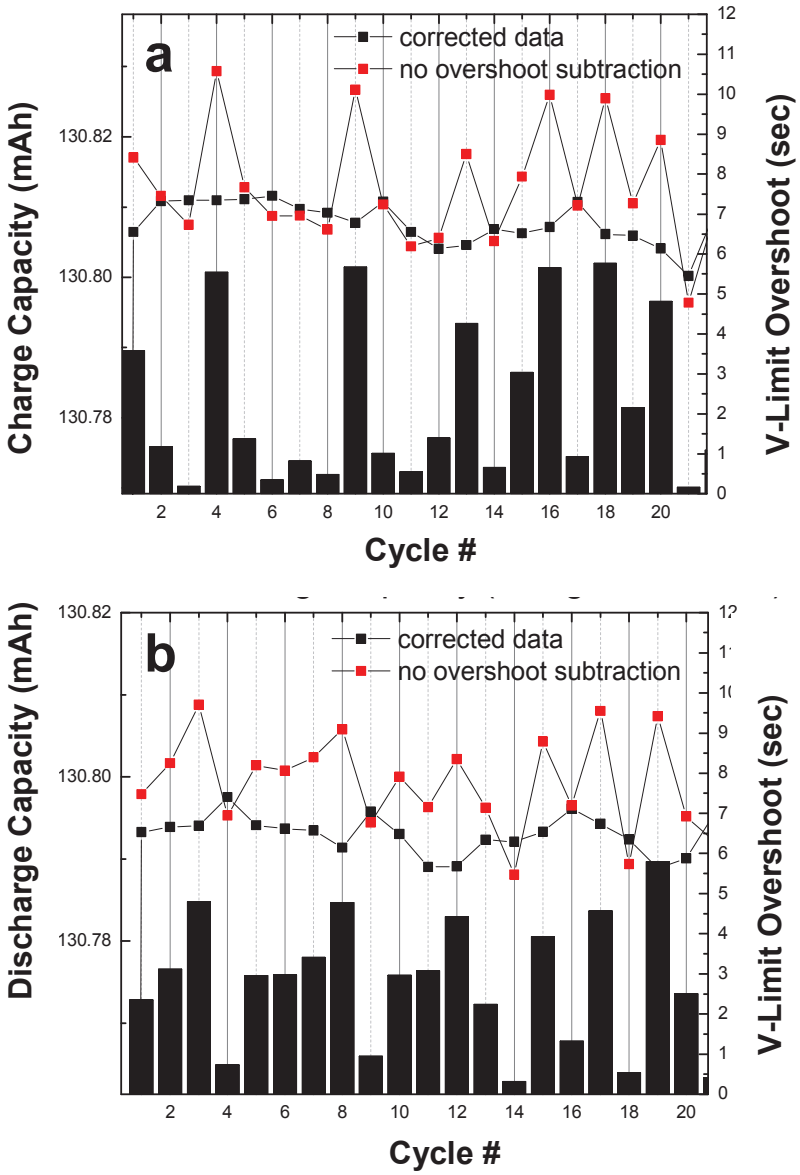

Figure 5.9 **a)** Correlation of charge capacity data to the corresponding overshoot of the discharge voltage limit. **b)** Correlation of discharge capacity data to the corresponding overshoot of the charge voltage limit. The voltage limit overshoot data is shown on the overlaid bar graphs and is expressed as the time interval (in seconds) over which a cell is charged/discharged past a given voltage limit.

The uncorrected capacity data in these plots follows the same contour as the voltage limit overshoot. This is to be expected, as a larger degree of overshoot will result in a greater amount of excess charge being transferred, increasing the uncorrected capacity value

(whereas a smaller degree of overshoot will not). However, the corrected capacity data also exhibited a correlation to the amount of voltage limit overshoot, only the relationship was inverted (a large overshoot resulted in a lower capacity value, while a small overshoot resulted in a greater capacity value). This correlation further indicates that the subtraction of excess charge appears to be overcompensating to some degree.

These correlations were observed for all 3 cells when cycled at a lower sample rate, (1 point per 6 seconds) but were not observed when the same cells were cycled at the fastest sample rate (1 point per 1.7 seconds). This data shows that there is a significant benefit to increasing the data sample rate, despite the endpoint correction that is in place. Changes to the endpoint correction procedure may yield improvements in CE precision without the need for hardware changes to the charger system. Some recommendations are discussed in Chapter 6.

5.3 Preliminary 2-Stage Cycling Using the UHPC

All of the data presented to this point was collected using cells that were cycled at a rate of C/10. For the study of phenomena such as electroplating of Li metal, faster charging rates are required. When cells are cycled using greater currents, problems arise due to solution resistance of the electrolyte in the cell. Solution resistance (the resistance due to "friction" encountered by ions as they move through solution) results in a voltage drop that is proportional to current. The result is a voltage curve which is shifted in the direction of the applied current, (positive shift when charging, negative shift when

discharging) making it increasingly difficult to obtain accurate capacity and CE data as the charging rate is increased.

One way to circumvent this problem is to use a 2-stage charging protocol. In 2-stage cycling, a cell is charged at a fast rate until it approaches a voltage limit, at which point the current is reduced to a smaller "top-up" current. This smaller current reduces the shift in voltage due to solution resistance, allowing for accurate charge and discharge to the appropriate voltage limits. An example of a 2-stage cycling experiment is shown in Figure 5.10.

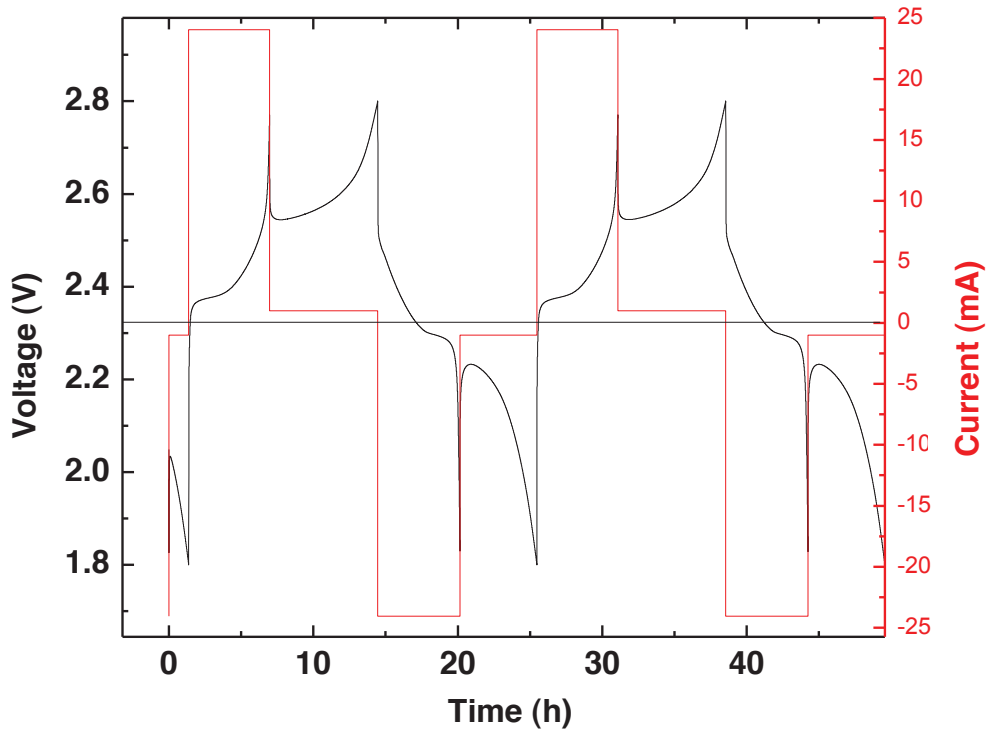

Figure 5.10 Voltage and current data from a 2-stage cycling experiment that was run on the UHPC. A commercial LTO/LCO cell was cycled at rate of C/5 with at top-up current of C/120.

When the current in this experiment was switched from 24 mA (a rate of C/5 for this cell) to 1 mA, (C/120) the result was a visible reduction in the voltage shift due to solution

resistance. This was followed by a gradual change in cell voltage as the cell was charged/discharged at a low rate to the appropriate voltage limit.

For Single-stage charging, it is more important that charge and discharge currents are balanced than it is for current output to be accurate with respect to the setpoint value. However, for 2-stage cycling, current accuracy becomes more of an issue. Figure 5.10 shows that the time interval over which the top-up current is applied is significantly different for charge and discharge. This makes accurate capacity calculations difficult if the exact current values are not known.

Two-stage experiments that were previously carried out using the HPC yielded CE results with large channel-to-channel variation, some of which remained well above unity. This problem should not be an issue if measured current is used, as current inaccuracy can be accounted for and corrected.

The UHPC was used to perform a preliminary 2-stage current experiment. A pair of commercially manufactured LTO/LCO cells from Medtronic Inc. were cycled over a range of 1.8-2.8 V using a principle charging rate of C/5 and a top-up current of C/120 (the data shown in Figure 5.10 was taken from this experiment). The top-up current was applied when the cell was charged/discharged to within 30 mV of the appropriate voltage limit. The resulting CE data and RMS error are shown in Figure 5.11.

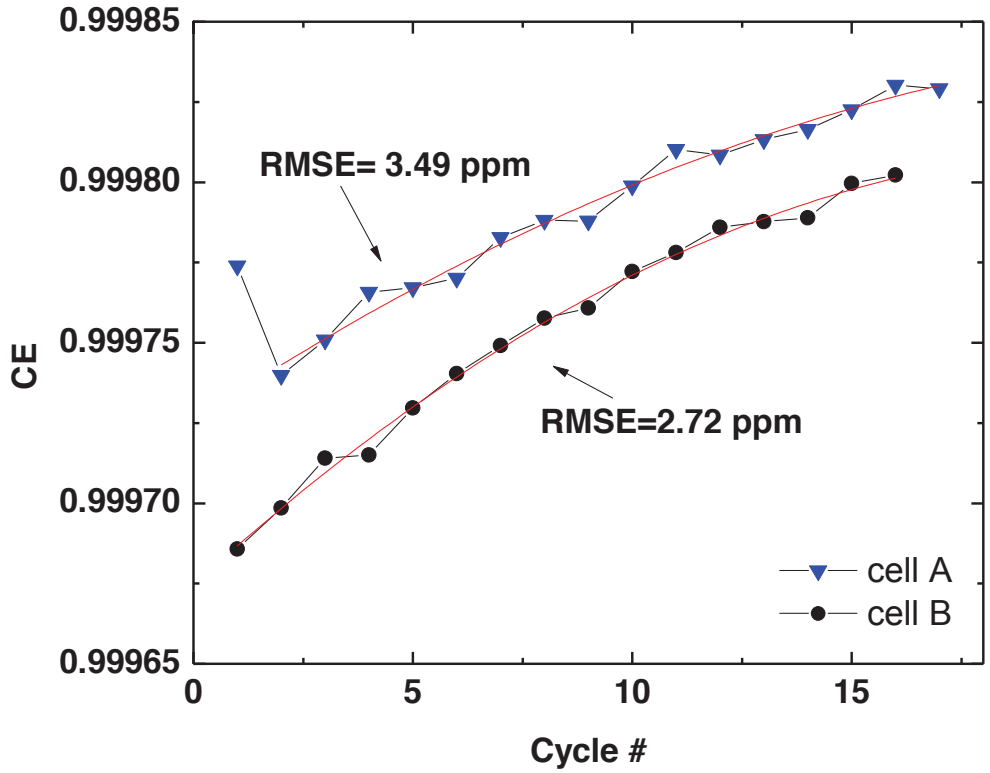

Figure 5.11 CE data and RMSE from a 2-stage experiment performed on the UHPC using 2 Medtronic LTO/LCO cells cycled at a rate of C/5 with a top-up rate of C/120.

This CE data displayed a particularly low degree of scatter as well as a low channel-to-channel variation of 25 ppm. Other 2-stage experiments discussed in the next section also yield reduced scatter compared to single-stage CE data. This may be the result of reduced voltage limit overshoot for 2-stage experiments, as the application of a much smaller current when crossing voltage limits would result in less charge being transferred in excess of the limit. The results from this preliminary test on the UHPC indicate that very precise and accurate 2-stage cycling can indeed be carried out when measured current is used.

5.4 Results of Other Charger Systems

In order to compare the performance of the UHPC to other chargers, 2 other systems were also characterized. One of these was a Maccor Series 4000 charger system which is a large-scale commercial charger system. This system represents the high end of commercially available charger systems. The other charger that was evaluated is a single-channel prototype of a high-precision "add-on" that was provided by A and D Technologies Inc. This add-on consists of a voltmeter and current meter integrated into a single unit. This unit is used in combination with an external current source or charger system (hence the term "add-on"). A picture of the A and D prototype is shown in Figure 5.12.

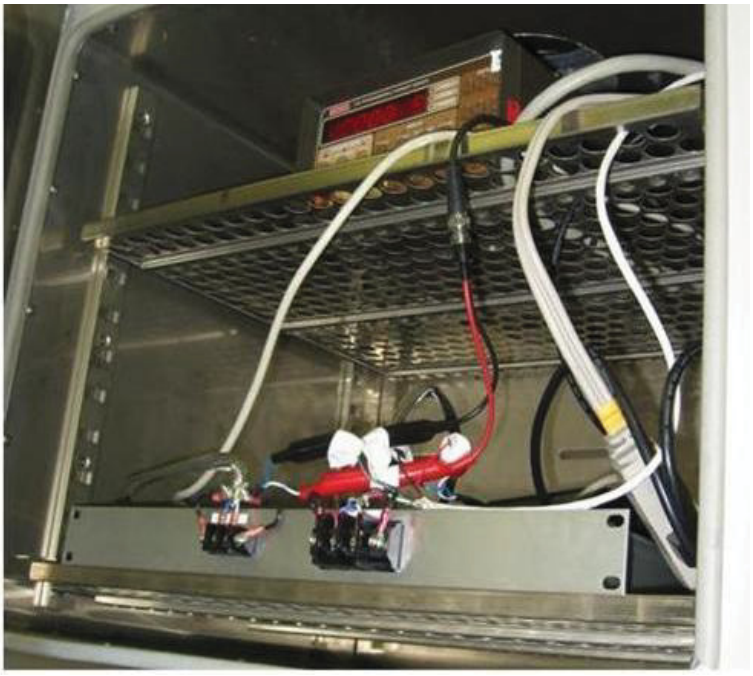

Figure 5.12 Prototype of a high-precision add-on provided by A and D Technologies Inc. (bottom shelf) connected to a Keithley 220 current source (top shelf) housed inside a D600 oven.

The A and D add-on is shown here inside a Yamato D600 oven that was used to temperature control the add-on and Keithley 220 current source to which it was connected. The temperature variations inside the oven (with both instruments running) were measured to be within ±0.15 ºC. The single current source did not produce enough heat to necessitate a heat management system (unlike the 3-channel UHPC). Cells that were tested using this system were placed in the same temperature control boxes used by the HPC.

In order to characterize the Maccor Series 4000 charger, two experiments were carried out using a set of "identical," newly manufactured commercial graphite/LCO cells. One set of cells was cycled using a current of 6 mA (which lies near the bottom of the Maccor charger's 150 mA range) while the other set was cycled at 4 mA (near the top of the charger's 5 mA range). The Series 4000 performs better near the top of a given current range, so this was done to show the upper and lower limits of the charger's performance. Figure 5.13 shows the resulting CE data from both of these experiments

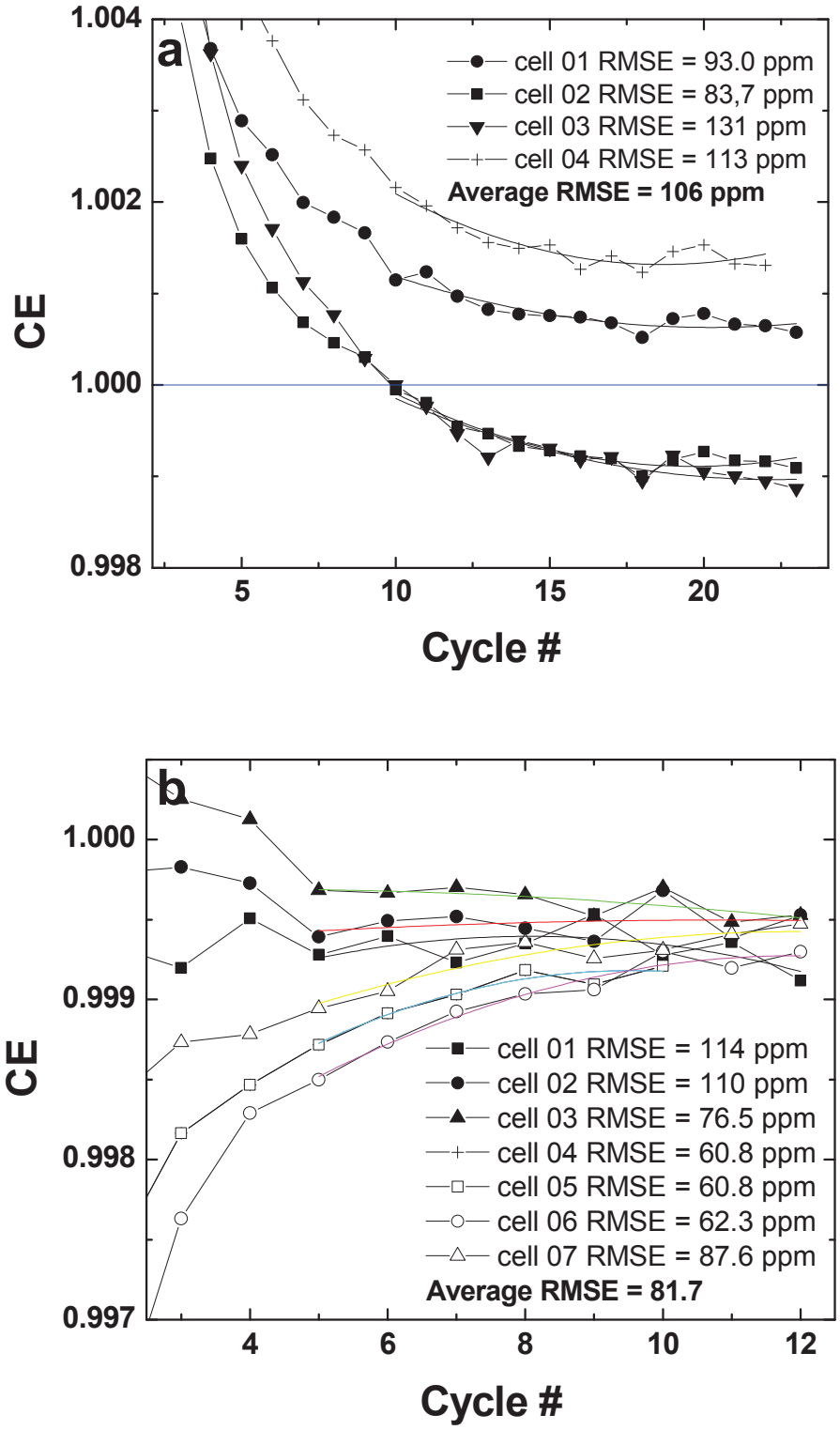

Figure 5.13 CE and RMSE of graphite/LCO cells cycled on a Maccor Series 4000 charger. **a)** Cells cycled using a current of 6 mA (bottom of 150 mA range) **b)** Cells cycled at 4 mA (top of 5 mA range).

The average RMS error values of each experiment are 106 ± 19 ppm for the low range experiment and 82 ± 23 ppm for the high range experiment (with errors corresponding to one standard deviation). The difference between these averages is significant with a confidence of 80%. The average RMS error of these two experiments is 93.9 ppm, which can be regarded as a typical amount of CE scatter expected for this charger. The channel-to-channel variation of the Series 4000 was also very significant, with the high-end results spread over a range of 658 ppm. The channel-to-channel variation of the low-end data was 2280 ppm, (0.228%) some of which remained above unity for the entire experiment. This accuracy is inadequate for the characterization of cells like the ones shown here, where CE values are very close to unity. The average of these two ranges is 1470 ppm (0.147%) which is well over an order of magnitude greater than the channel-to-channel variation seen for either the HPC or UHPC. Calculation of capacity data was handled by proprietary Maccor software, so details regarding data processing and endpoint handling are not known.

A 2-stage experiment was also carried out on the Series 4000 using 4 of the above graphite/LCO cells. The cells were cycled at 24 mA (C/4) with a top-up current of 1 mA (C/100). The results of this experiment are shown in Figure 5.14.

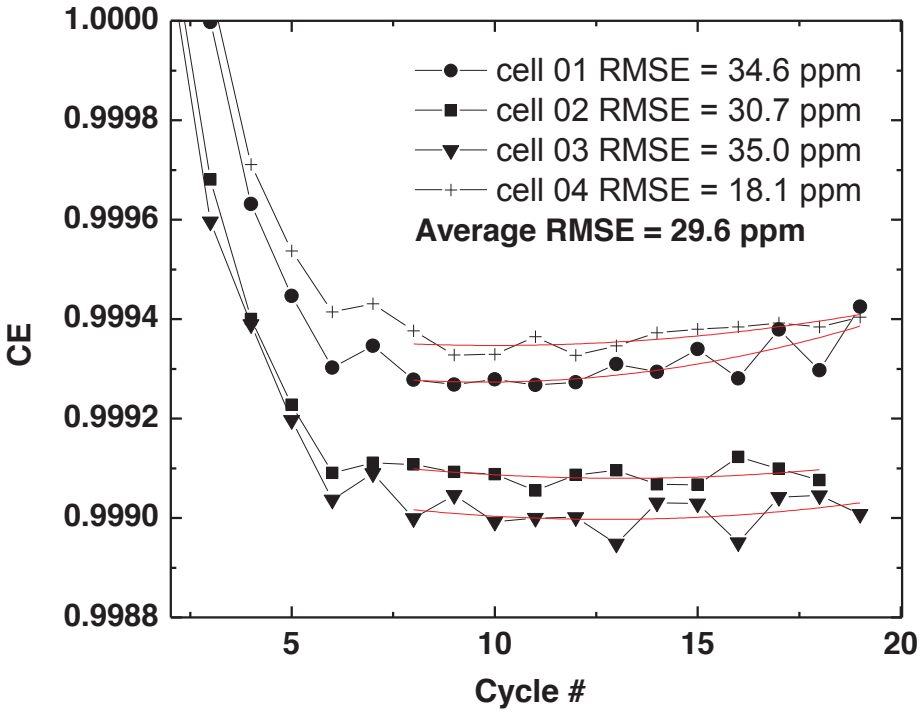

Figure 5.14 CE data from a 2-stage experiment carried out on the Maccor Series 4000 charger, using 4 of graphite/LCO the cells shown in Figure 5.13.

The CE scatter of this data is greatly reduced compared to the single-stage data in Figure 5.13. As previously mentioned, this is likely due to more accurate endpoint determination resulting from the comparatively small current that is applied when approaching voltage limits. The channel-to-channel variation, though improved, is still quite large at 367 ppm.

The A and D high-precision add-on was tested with a Keithley 220 current source using a Medtronic LTO/LCO cell. 2 experiments were carried out to examine this system's single- and 2-stage precision, using the same charging rates and cell temperatures as previously described UHPC experiments (see Sections 5.1 and 5.3). The results of these tests are shown in Figure 5.15.

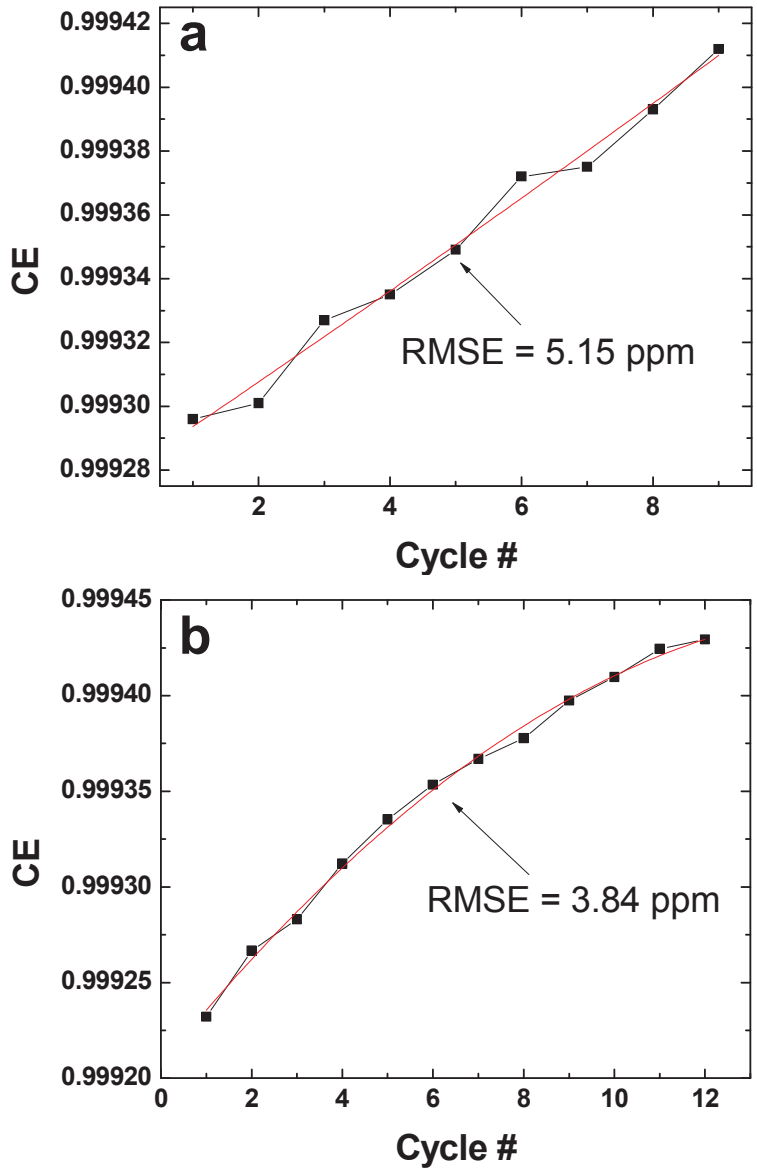

Figure 5.15 CE data from **a)** single-stage and **b)** 2-stage experiments that were performed using the A and D high-precision add on and Keithley 220 current source.

Capacity and CE calculations were carried out using the same software used for processing UHPC data. These results indicate that the precision of this system is essentially equivalent to that of the UHPC for both single- and 2-stage. The A and D add-on samples data at a rate of 6 points per second, which is much faster than the HPC

or UHPC (resulting in output files that frequently exceeded 1 GB). It is interesting to note that, despite this greatly increased sample rate, there appear to be no further benefits in terms of CE precision.

The A and D add-on displayed excellent precision when used with the Keithley 220 current source, but it remained to be seen how it would perform when used with a much noisier current source. To investigate this, the A and D add-on was connected to the Maccor Series 4000 charger, which uses a current source that produces significantly noisier output than that of the 220. Figure 5.16 shows the discharge current output from both of these sources for comparison.

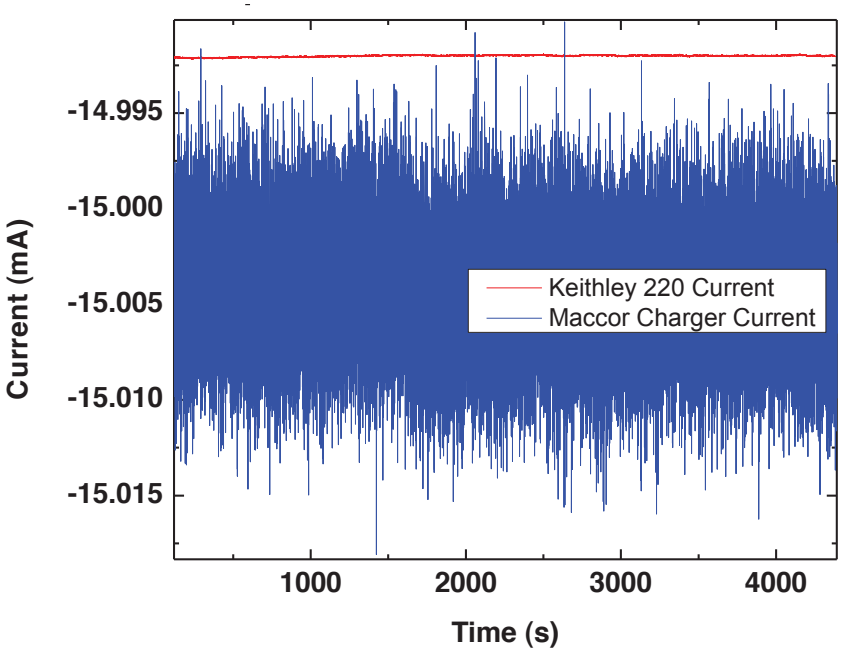

Figure 5.16 A sample of discharge current output measured from a Keithley 220 current source and the Maccor Series 4000 charger. Both instruments were set to supply 15.000 mA.

When linear regression was applied to this data, the resulting RMS error of the Maccor charger's current output was 214 ppm, compared to only 3.4 ppm for the Keithley 220 (almost 2 orders of magnitude noisier). For these experiments, the current source was controlled by the Maccor charger's operating software and the A and D add-on was used to monitor cell voltage and current output from which capacity and CE data were calculated. A Medtronic LTO/LCO cell (cycled at a cell temperature of 30 ºC) was used to conduct a single-stage and 2-stage experiment. The cell was cycled at a rate of C/10 for the single-stage experiment, while the 2-stage experiment was carried out using a rate of C/5 with a top-up rate of C/120. The results of these experiments are shown in Figure 5.17.

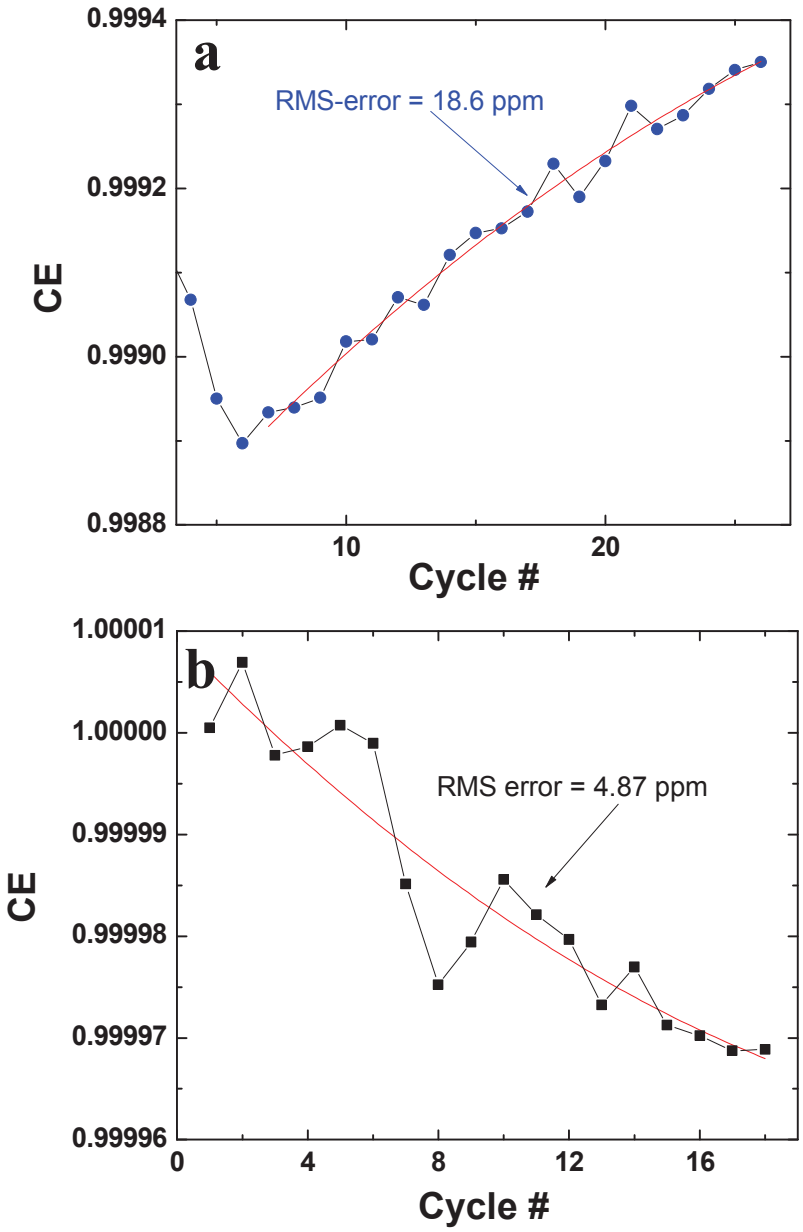

Figure 5.17 **a)** Single-stage and **b)** 2-stage CE data from experiments that were conducted using the Maccor Series 4000 charger with a high-precision add-on made by A and D Technologies.

Both of these experiments showed a significant improvement in CE precision compared to the results obtained using the Maccor charger alone. The scatter of the 2-stage CE data was comparable to that of the 2-stage data obtained using the Keithley 220. However, the scatter of the single-stage data was approximately 4 times worse than that of the

experiment performed with the Keithley 220. Although the A and D add-on was shown to improve the performance of a less-precise charger, it would appear from these results that a low-noise current source is still required in order to achieve optimal precision for single-stage charging.

5.5 Summary

The effect on CE precision of measured current, temperature control of instruments, stabilization of power source voltage, and sample rate were all investigated in detail. When current sources were not temperature controlled, output became visibly noisier, resulting in increased CE scatter. The measurement of this noisier current provided an effective means of offsetting this increase in scatter. The use of measured current was also shown to improve CE accuracy, as imbalances in charge/discharge currents could be corrected for. The use of voltage stabilization appeared to have no effect on CE precision.

The increased sample rate of the UHPC also contributed to a reduction in CE noise. When the sample rate of the UHPC was decreased, variation in CE data could be correlated to variation in the amount of voltage limit overshoot. The sample rate of current measurement was also examined using software post-processing, and it was determined that a sample rate of approximately 1 data point per 2 minutes would provide sufficiently precise results.

The performance of a Maccor Series 4000 charger and a high-precision add-on from A and D Technologies were both evaluated. The Series 4000 yielded CE data with

an average RMSE of 82 ppm. The A and D add-on showed performance equivalent to that of the UHPC when used with a Keithley 220 current source. When the A and D add-on was used in combination with the Series 4000, (which is a much noisier current source than the Keithley 220) there was a significant improvement in precision compared to the results obtained from the Series 4000 alone. However, the single-stage data acquired with the Maccor/A and D system still contained a high level of scatter compared to the data collected using the same add-on with a Keithley 220 current source. The next chapter summarizes the general conclusions of this thesis and discusses possibilities for future work.

CHAPTER 6 CONCLUSIONS AND FUTURE WORK

6.1 CONCLUSIONS

As the use of Li-ion batteries in applications like electric vehicles and grid storage becomes increasingly widespread, the development of longer-lasting batteries becomes essential. The lifetime of Li-ion batteries is limited by parasitic reactions occurring within the cell. CE is an important tool for characterizing new batteries, as it provides a means of quantifying the magnitude of these parasitic currents. As more stable batteries are developed, the level of parasitic current is reduced, resulting in CE that is increasingly closer to unity. In order to resolve minute differences in CE between cells, a higher degree of precision and accuracy in CE measurement is required.

The HPC at Dalhousie University was constructed in 2009 to address this need. The HPC demonstrated precision in CE measurements well beyond that of commercially available chargers (yielding CE data with RMS error just below 20 ppm). The UHPC was constructed using the same instrumentation as the existing HPC. The UHPC contained four modifications to the design of the existing HPC, namely: the measurement of current source output, temperature control of instruments, voltage stabilization of instrument power supply, and increased sample rate.

With these modifications in place, the UHPC yielded CE data that was approximately four times more precise than the existing HPC, with RMS error that was reproducibly below 5 ppm. Several experiments were carried out to examine the effect of each modification in detail. It was found that the removal of instrument temperature

control resulted in more CE scatter due to increased noise in current source output. However, when measured current data was used to calculate CE, (as opposed to assuming constant current output) this noisier current could be accounted for and the increase in CE scatter was mostly eliminated. The other significant advantage to measuring current was that it improved CE accuracy by correcting for imbalances between charge and discharge current output. The voltage stabilization of power supplied to instruments did not show any significant improvement.

The effect of data sample rate on current measurement and voltage limit overshoot were investigated separately. Using software post-processing, it was determined that there was no change in CE scatter when current was measured at a rate of 1 data point every 2 minutes. However, as current sample rate was further reduced, CE scatter gradually increased until it reached a maximum that was almost equal to the scatter yielded by constant-current calculations. Although CE precision suffered as the current sample rate dropped, there was no shift in the measured current CE, even when a sample rate of 1 point per charge/discharge was used.

When the sample rate of the UHPC was physically lowered to the rate used by the existing HPC, a significant increase in CE scatter was observed. The variations in CE and capacity of the lower-sample-rate data showed a strong correlation to the degree of voltage limit overshoot (a correlation that was not observed for the faster-sample-rate data). The data also suggested that the endpoint interpolation/correction procedure currently used appeared to overcorrect for charge that was transferred in excess of voltage limits.

The performance of the UHPC was also compared to the performance of other charger systems, namely, a Maccor Series 4000 charger and a high-precision add-on manufactured by A and D Technologies. The Series 4000 yielded CE results with scatter that was below 100 ppm, but accuracy was comparatively poor, as differences in CE between channels ranged from 500 ppm to 0.25%. The performance of the A and D add-on was on par with that of the UHPC for both single- and 2-stage experiments when it was used with a Keithley 220 current source. When the add-on was attached to the Series 4000, the precision was greatly improved with respect to the performance of the Maccor charger alone. However, the single-stage data obtained using the combined Maccor/A and D system was approximately four times noisier than the data obtained using the A and D add-on with the Keithley 220 source. Figure 6.1 shows an overall comparison of the precision and accuracy demonstrated by each charger system discussed in this thesis.

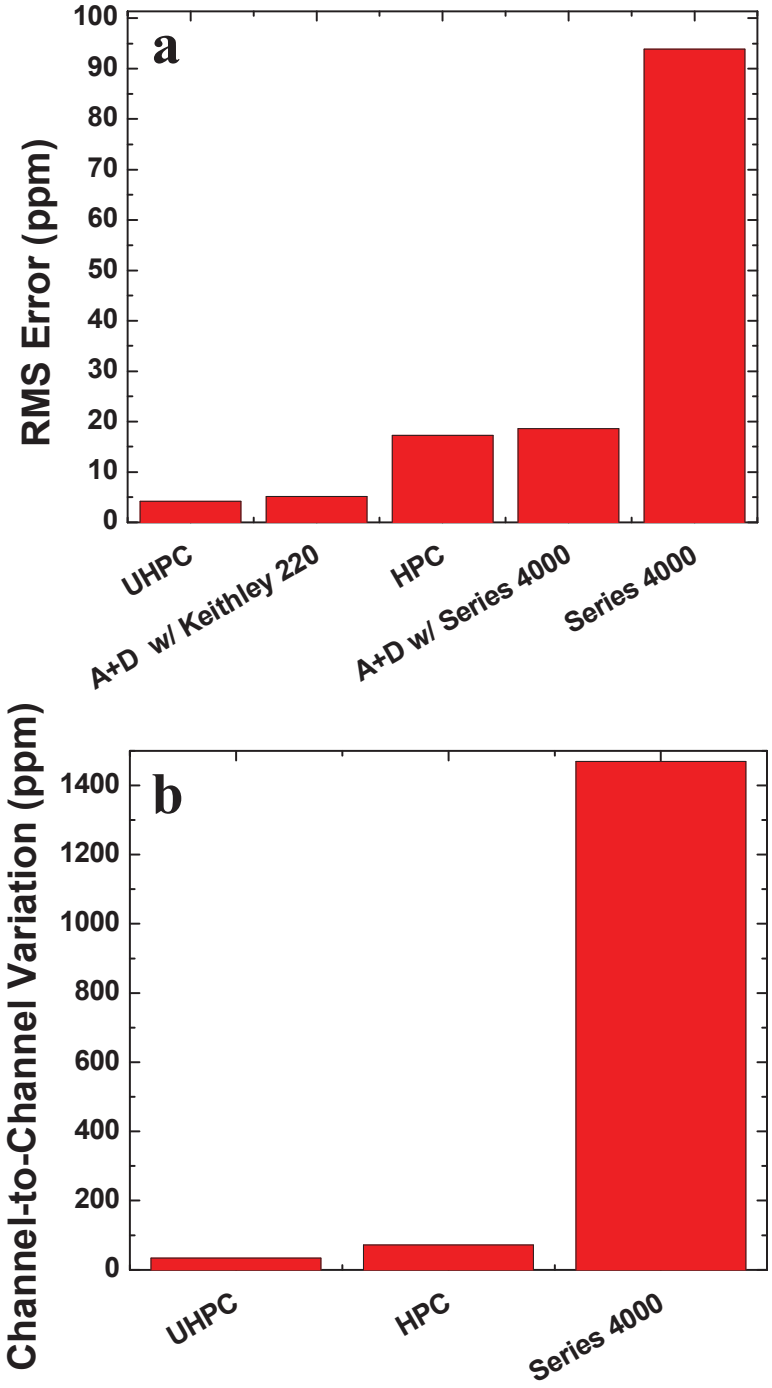

Figure 6.1 **a)** The precision of all chargers discussed in this thesis, which is indicated by the average (where appropriate) RMS error of CE data. "A+D" refers to the high-precision add-on provided by A and D Technologies that was used with an external current source as indicated. **b)** The accuracy of all multi-channel chargers discussed in this thesis, which is indicated by Channel-to-channel variation (calculated as described in Section 3.3)

The UHPC and A and D add-on (used with a Keithley 220) have demonstrated that a charger system constructed with high-precision components that utilizes measured current, sufficiently high sample rate, and temperature control of instruments can yield a precision in CE that is more than an order of magnitude better than that of a high-end commercial charger. The channel-to-channel variation of the UHPC was measured (from a single 3-channel experiment) to be 33.2 ppm, which is about twice as good as the variation of the HPC, and almost two orders of magnitude better than the variation of the Maccor Series 4000 charger. As discussed in Chapter 3, the term "channel-to-channel variation" refers to what is in fact the combined result of both channel-to-channel and cell-to-cell variation. It is not known how much cell-to-cell variation contributes to the above-mentioned values, but the difference in CE between cells must be some value less than 33.2 ppm (for the commercial cells used in this thesis). It may be that the majority of this "channel-to-channel" variation is in fact due to differences between cells, but this cannot be known for certain.

6.2 Ongoing and Future Work

This thesis has provided a set of design principles that can be used for the construction of new charger systems, as well as for the modification of existing ones. The most important modification implemented was the use of measured current, as it provided for both increased precision and accuracy. The increased sample rate also yielded a significant improvement in precision. Though the use of instrument temperature control also showed improved precision, it is comparatively difficult and

expensive to implement. The use of measured current and increased sample rate is presently being implemented in the design of new charger systems in the Dahn lab.

In order to improve the performance of the existing HPC, modifications are currently underway to increase data sample rate and enable the measurement of current . In order to achieve this, each 10-channel subsystem of the 60-channel HPC will use four Keithley 2000 DMMs instead of one. Each pair of DMMs will be used to monitor five channels, where one DMM will be dedicated to measuring cell voltage while the other will be dedicated to monitoring current (using the same high-precision resistors as the UHPC). Figure 6.2 shows a 10-channel subsystem which has already been modified in this way.

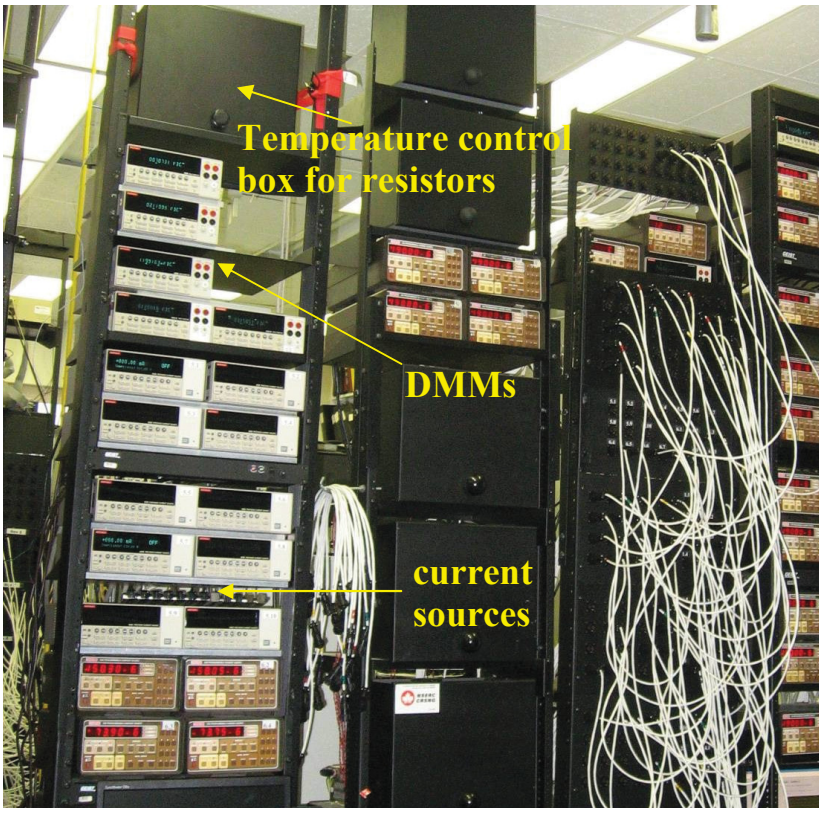

Figure 6.2 A 10-channel subsystem of the existing HPC that has been modified to measure current and increase maximum data sample rate.

Since each pair of DMMs monitors only 5 channels instead of 10, the maximum sample rate is effectively doubled. Each channel has a dedicated array of high-precision resistors installed in a relay system (built by David Stevens) that can select a suitable resistor based on the current output of a channel without having to swap out the resistor manually. These resistor relays are housed in a temperature control box (indicated in Figure 6.2). New software to control this modified system has been written in Visual Basic by David Stevens and Hannah Dahn. Initial experiments are currently underway, and the remaining subsystems of the HPC will be sequentially modified in a similar manner.

The Dahn lab has received funding from the NSERC Automotive Partnership Canada to build an ultra high precision charger system that is capable of running large-scale cells intended for use in electric vehicles. This charger is currently under construction, and is also designed to measure current using a similar setup to the modified HPC. In order to provide a sufficient amount of current for large-scale cells, the charger will use Keithley 2602 current sources which can output up to 3 A (compared to the 100 mA maximum of the Keithley 220). The measurement of cell voltage and current for this system will be carried out using Keithley 2002 DMMs, which have an 8.5-digit resolution (compared to the 6.5-digit resolution of the Keithley 2000) as well as a lower temperature coefficient.

Aside from hardware modifications, it will be useful to further investigate ways to refine the process of endpoint interpolation and correction. As discussed in Section 5.2.2, variation in capacity and CE data was correlated to voltage limit overshoot (when

sampling interval of 6 seconds was used) even though endpoint correction was in place. This suggested that improvements could still be made to the interpolation/correction procedure outlined in this thesis. One approach currently being investigated involves performing endpoint interpolation using several data points to form a line of best fit, as opposed to using only the last two data points and interpolating between them. This should provide a more accurate interpolation that would offset any potential problems due to voltage measurement error near voltage limits. Another possible approach would be to use non-linear fitting functions to account for any curvature that may be present as voltage limits are approached.

The fundamental purpose of increasing charger precision is to be able to resolve increasingly minute differences in CE between different cell chemistries. Once the above-mentioned modifications are complete, the improved precision and accuracy can be fully utilized to investigate additives and cell materials whose differences could not previously be resolved (such as those shown in Section 3.5). The results of the UHPC shown in this thesis were all obtained using LTO/LCO cells, so it will also be important to determine if the same level of precision can be demonstrated using other electrode materials.

REFERENCES

[1] T. Reddy, Linden's Handbook of Batteries, 4th ed. (McGraw- Hill Professional, 2010).

[2] J. R. Dahn, T. Zheng, Y. Liu, and J. S. Xue, Science 270, 590 (1995).

[3] T. Ohzuku, A. Ueda, and N. Yamamoto, J. Electrochem. Soc. 142, 1431 (1995).

[4] R. Koksbang, J. Barker, H. Shi, and M. Y. Saïdi, Solid State Ionics 84, 1 (1996).

[5] E.Peled, D. Golodnitsky, and G. Ardel, J.Electrochem. Soc, 144, L208 (1997).

[6] R. Fong, U. von Sacken, and J. R. Dahn, J. Electrochem. Soc. 137, 2009 (1990).

[7] Kang Xu, Chem. Rev. 104, 4303 (2004).

[8] A. J. Smith, J. C. Burns, D. Xiong, J. R. Dahn, J. Electrochem. Soc. 158 A1136 (2011).

[9] J. Vetter, P. Novák, M. R. Wagner, C. Veit, K.C. Möller, J. O. Besenhard, M.Winter, M. Wohlfahrt-Mehrens, C. Vogler, and A. Hammouche, J. Power Sources 147, 269 (2005).

[10] T. Ohzuku, A. Ueda, N. Yamamoto, Y. Iwakoshi, J. Power Sources 54, 99 (1995).

[11] M. Q. Li, M. Z. Qu, X. Y. He, and Z. L. Yu, J. Electrochem. Soc. 156, A294 (2009).

[12] T.F. Yi, C.Y. Li, Y.R. Zhu, J. Shu, and R.S. Zhu, J. Solid State Electrochem. 13, 913 (2008).

[13] A. J. Smith, J. C. Burns, S. Trussler, J. R. Dahn, J. Electrochem. Soc. 157, A196 (2010).

[14] J. R. Dahn and R. R. Haering, Can. J. Phys. 61, 1093 (1983).

[15] Deijun Xiong, J. C. Burns, A. J. Smith, Nupur Sinha, and J. R. Dahn, J. Electrochem. Soc. 158, A1431 (2011).

[16] J. C. Burns, N. N. Sinha, D. J. Coyle, Gaurav Jain, Collette M. VanElzen, W. M. Lamanna, A Xiao, Erik Scott, J. P. Gardner, and J. R. Dahn, J. Electrochem. Soc. 159, A85 (2012).